Aircraft and Rotorcraft Pilot Couplings – Tools and Techniques for Alleviation and Detection

ACPO-GA-2010-266073

Deliverable No. D4.10
Report detailing the new/updated rigid body RPC prediction criteria

Contractual delivery date:
July/2013

Actual delivery date:
August/2013

Partner responsible for the Deliverable: ONERA

Author(s):
Binh Dang-Vu (ONERA),
Lu Linghai (UoL), Michael Jones (UoL), Michael Jump (UoL),
Marilena D. Pavel (TUD), Deniz Yilmaz (TUD)

Dissemination level		
PU	Public	
PP	Restricted to other programme participants (including the Commission Services)	
RE	Restricted to a group specified by the consortium (including the Commission Services)	
CO	Confidential, only for members of the consortium (including the Commission Services)	X

Document Information Table

Grant agreement no.	ACPO-GA-2010-266073
Project full title	ARISTOTEL – Aircraft and Rotorcraft Pilot Couplings – Tools and Techniques for Alleviation and Detection
Deliverable number	D4.10
Deliverable title	Report detailing the new/updated rigid body RPC prediction criteria
Nature	R[1]
Dissemination level	CO[2]
Version	1.0
Work package number	WP4
Work package leader	UoL
Partner responsible for Deliverable	ONERA
Reviewer(s)	

The research leading to these results has received funding from the European Community's Seventh Framework Programme (FP7/2007-2013) under grant agreement n° 266073.

[1] **R**=Report, **P**=Prototype, **D**=Demonstrator, **O**=Other

[2] **PU**=Public, **PP**=Restricted to other programme participants (including the Commission Services), **RE**=Restricted to a group specified by the consortium (including the Commission Services), **CO**=Confidential, only for members of the consortium (including the Commission Services)

Revision Table

Version	Date	Modified Page/Section	Author(s)	Comments
1.0	26.07.13		See list	
2	22.08.13		See list	

Executive Summary

This document presents a summary of the new criteria and analysis methods developed in the ARISTOTEL project for the prediction of RPC. It is based on the synthesis of the revised database of RPC predictions reported in Deliverable D2.7, the simulator test data analyses of the 1st and 2nd test campaigns reported in D4.6 and D4.8, and the validation exercise reported in D4.9.

Table of Contents

1. Introduction

Through WP2 and WP4 and in accordance with the Description of Work document [1], the current existing RPC prediction criteria have been assessed, and new predictive criteria have been developed and validated. The adopted three-pronged approach – analysis, off-line simulation, simulator experiment – has indeed led to the generation of a theoretical prediction database [2], the generation of an experimental database [3;4], and the assessment of traditional and newly developed RPC criteria using the tests data of a 1st simulator test campaign performed on the SIMONA and the HELIFLIGHT-R simulators [5]. The 2nd simulator test campaign provided additional data that were used to update the validation of the RPC criteria. The subject of the present document is to make a synthesis of the results concerning RPC rigid body prediction, with a focus on new RPC criteria and analysis methods.

2. Summary of Work Performed

The summary of work contains the following sections:

- Prediction based on Enhanced Real-Time Oscillation Verifier (TUD)
- Prediction using the Phase-Aggression Criterion (UoL)
- Prediction based on Boundary Avoidance Tracking (UoL)
- Prediction based on Optical Tau (UoL)
- Prediction based on Bifurcation Analysis (ONERA).

2.1 Prediction based on Enhanced Real-Time Oscillation Verifier

For real-time detection, a Real-Time Oscillation VERifier (ROVER) was developed more than a decade ago for the U.S. Air Force [6;7]. This initial ROVER algorithm was applied only to fixed wing aircraft. Since the first development, ROVER has been refined and assessed in ground based simulation campaigns. It has been applied to fixed wing aircraft by the GARTEUR AG 12 [8] and to rotorcraft in Italy [9]. A major drawback of ROVER is that it can be prone to false alerts. For example the classical ROVER algorithm was able to detect correctly only 34 per cent of the cases whenever the pilot did not observe an APC. Besides, both the pilot and the ROVER detected an APC in 91 per cent of the cases. Perhaps a much cumbersome issue is the fact that users can select their own thresholds for PIO detection. If these are not set correctly, significant over/under prediction will occur. Therefore, there is a need for improvement of the ROVER algorithm and this was done in the ARISTOTEL project. This section revises the classical ROVER algorithm and explains the improvements added to the algorithm in order to cope with false alerts in the algorithm.

Classical Rover Algorithm

The ROVER algorithm for fixed wing aircraft was first developed by Mitchell et al. around 2000 [6;7]. The fundamental assumption in ROVER is: *'There is no such thing as "pre-PIO" condition: PIO will never be prevented in real-time, so the best we can hope to do is detect it early and minimize the effect on the aircraft'*. [7]. Figure 1 presents the classical ROVER algorithm.

Mainly, two inputs are used in ROVER: 1) pilot control stick input and 2) body angular rate response. The algorithm gives three outputs: 1) the peak-to-peak amplitudes 2) the frequency of body rate and 3) the phase delay between the stick input and body rate. The main idea is that every time a peak in angular rate is detected, the time between the current and previous peaks is used to compute oscillation frequency (the assumption is that the peak-to-peak response is a half-cycle of a sine wave). If this frequency is in the range associated with PIO, a **first flag** is set. A **second magnitude flag** is set if the peak-to-peak amplitude is above the threshold for PIO. The time between peaks in angular rate is compared to the time between peaks of the most recent past stick oscillation, the time difference is converted to phase angle using the frequency determined from the rate response, and if this phase angle is in the range for PIO, **a third flag** is set. The **fourth and final flag** is set if the peak-to-peak control input amplitude is above a predefined threshold value. Severe PIO requires that all 4 flags are set for a single half-cycle of oscillation and corresponds to a detected APC (PIO). When a score 3 happens and there is rate limiting, the angular rate can be suppressed by the rate limiting. Two consecutive scores of 3 and 3.5 score result in an APC warning. One can therefore conclude that pre-defined threshold values must be set by the user for the angular rate and also for the control input. Only in this condition ROVER is capable of detecting severe PIO in the first half-cycle. Discussing on these thresholds, at TUD it was observed that the threshold values of peak selection method, depend on: 1) The order of the filter as well as the cut-off frequency and 2) The system dynamic behaviour: When changing the time delay, to get a reliable peak picking, the thresholds need to be adjusted for each trial configuration. This also means that for a longitudinal task most likely the threshold values are different than a lateral task, depending on the vehicles response margin in longitudinal axis.

Rotorcraft thresholds for peak selection were chosen at TUD after inspection of the simulator trials of the 1st test campaign performed for different time delays. The threshold values for the ROVER output have been determined by inspection of the output of the calculated amplitude, frequency and phase delay. The thresholds used by TUD and other versions of ROVER are presented in

Table 1. This is one of the shortcomings of ROVER, i.e. the threshold values are dependent per flight task, helicopter and configuration.

Table 1: Threshold values for ROVER as defined at TUD

Threshold name	*Value*	*Unit*
Stick amplitude	2.5	reg
Roll rate amplitude	18	reg/s
Frequency	1 to 8	rad/s
Phase delay	75	deg
Peak selecting threshold	*Value*	*Unit*
Δstick extreme	0.2	deg
Δtime stick extreme	0.3	sec
Δroll rate extreme	1.2	deg/s
Δtime roll rate extreme	0.3	sec

ROVER threshold values used in original algorithm (Johnson, 2002 [41])

	Basic	Improved

Pitch rate	> 12 deg/s	> 15 deg/s
Stick amplitude	> 5 deg	> 4 deg
Phase delay	> 65 deg	> 105 deg
Oscillation frequency	1 to 8 rad/s	1 to 8 rad/s

ROVER threshold values used at Agusta Westland (Mariano, 2011 [9])

Pitch rate	> 40 deg/s
Stick amplitude	> 15 deg
Phase delay	83 to 97 deg
Oscillation frequency	1 to 8 rad/s

ROVER threshold values as used at UoL (Jones, 2012 [11])

Pitch rate	> 12 deg/s
Stick amplitude	> 1.5 (20%) inches (of full travel)
Phase delay	60 to 120 deg
Oscillation frequency	1 to 8 rad/s

For the ROVER algorithm, it should be mentioned that it is also possible to have severe PIO with only three of the flags set; for example, if rate limiting is present, there can still be out-of-phase oscillatory response, but angular rate will be suppressed by the rate limiting. ROVER has additional tests for this sort of condition. The two prerequisites for PIO, in any case, are frequency of oscillation in the range for PIO and aircraft out of phase with the pilot.

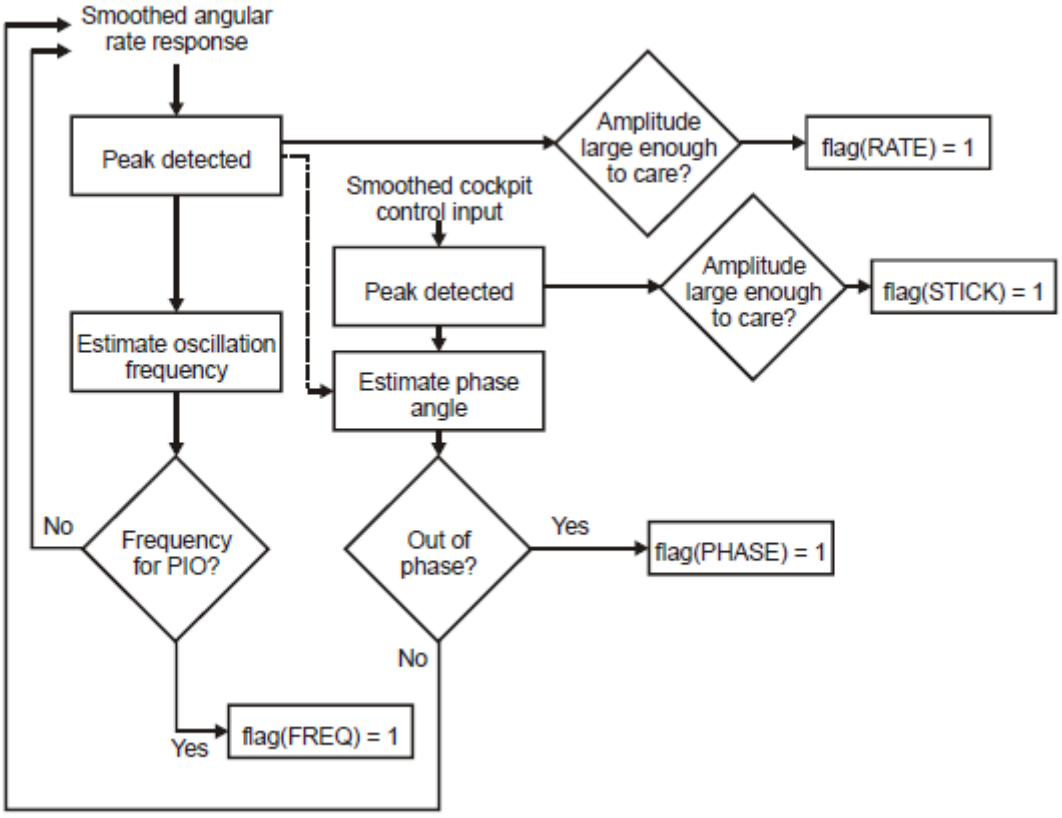

Figure 1: ROVER algorithm [7].

As mentioned above within the ROVER algorithm, first the stick and body input are filtered to remove high frequency oscillations and prevent issue of unrealistic large phase delay detection. Usually, this is done using a third order Butterworth filter with a cut-off frequency of 8 rad/s to be able to observe oscillations of the body up to 8 rad/s. An example of a filtered and corresponding unfiltered signal is shown in Figure 2. As can be seen, high frequencies are removed and the extreme values are slightly reduced at some points. Although the Butterworth filter smoothens part of the signal, still the issuing of false flags is possible. To reduce this even further thresholds are applied for frequency of the body, amplitude of stick input and body and phase delay. Further peak selection logic is implemented to reduce false alerts. The next paragraphs give a brief explanation on this peak selection logic.

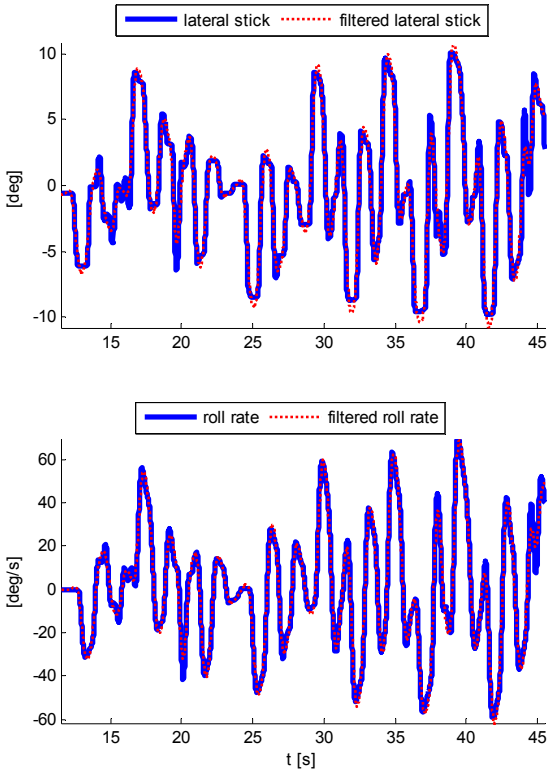

Figure 2: Original lateral stick and filtered lateral stick input.

In the classical ROVER algorithm the body rate response is used rather than the body attitude response. The reason to use rate response is twofold. First, the body angular response is small at the initiation phase of an A/RPC event making it difficult to detect motion of the body. Second, the angular response has non-zero mean. It is noted though that the phase delay during an A/RPC event is 90 degrees if the body angular rate is taken instead of the body angular motion. Using the stick input and the rotorcraft response as inputs, the algorithm calculates outputs: the amplitude and the frequency of the rotorcraft response and also the phase delay between the pilot and the rotorcraft response. Next, a short explanation is given how ROVER algorithm calculates these outputs.

Amplitude

The amplitude of the stick input and rotorcraft motion is calculated using the peaks of the motion with the following relation $ampl = \frac{peak_{curr} - peak_{prev}}{2}$. In this equation the amplitude of either the stick input or body rate response is based on the current and previous peak values of the signal. The peak values are determined by comparing consecutive extremes with so called *peak selection thresholds* for the time between extremes and difference of the magnitude of two successive extremes. When the *peak selection thresholds* are met the current extreme is considered a peak. Otherwise, the algorithm rejects the current peak and tries to find the next extreme value. This is how the calculation in the classical ROVER works. A simple method to reduce false flags is already accomplished by applying the following method. If the threshold values are met, the extreme is stored as a peak of the signal. If, on the other hand, successive extremes are within the limits for peak selection, then they are stored in an array after which the average becomes the peak value. This logic is applied in the ROVER algorithm implemented by Delft University of Technology (TUD). In this way the detection quality of ROVER is improved especially around peak values which oscillate around a maximum or minimum value.

Frequency

The frequency of the body motion is calculated by using the following equation $freq = \frac{2\pi}{t_{peak\_curr} - t_{peak\_prev}}$. Note that the frequency is based on the time of the current and previous peak. The calculation of the stick frequency can be calculated in an analogous way.

Phase delay

The phase delay is determined by calculating the time difference between corresponding minimum or maximum peaks of body and stick. Because of actuators in the system and the rotorcraft dynamics like low pass filters, not all stick frequencies result in a body response. The stick input is therefore noisier than the body response. During the simulation it is possible that multiple peaks of stick correspond to only one certain peak of the body. In this situation the average time of occurrence of the stick peaks are taken to perform the phase calculation. The phase delay is calculated using the following equation $phase = \frac{2\pi \cdot \Delta t}{freq_{body}}$ in which Δt is the time lag between the body peak and the stick peak. The calculated values of amplitude, frequency and phase delay are checked against threshold values and a score is issued dependent on the number of thresholds met. Thus, a maximum score of four is achievable and corresponds to a fully developed RPC detected event. If at two consecutive instances the score is three, the score is changed to 3.5 so a warning can be given to the pilot that he/she is approaching a RPC event.

Enhanced ROVER

Throughout benchmarking and evaluation phases of ROVER algorithm, at TUD it was observed that the original ROVER had difficulties to accurately detect RPC occurrences during some segments of sample scenarios. To accomplish better detection accuracy, the original algorithm was improved [10] by considering several peak selection adjustments as illustrated in

Figure 3 and Figure 4. After the stick input and aircraft roll rate are filtered, the algorithm determines the position of the “candidate” maxima and minima, as shown in

Figure 3. Three consecutive points are needed to determine if a point is a candidate minimum or maximum.

Figure 3: Candidate maximum and minimum in ROVER algorithm.

For selecting the peaks, an interval is used, so called peak selection thresholds (PST). If next candidate extreme is within the PST, in the classical algorithm the candidate is discarded and the algorithm continues. However, in TUD algorithm, all candidates are stored in an array and the resultant peak is calculated by averaging the candidate array. Thus, miscalculations of frequency and phase are reduced and a more robust peak selection was achieved. The difference between the two methods is illustrated in Figure 4.

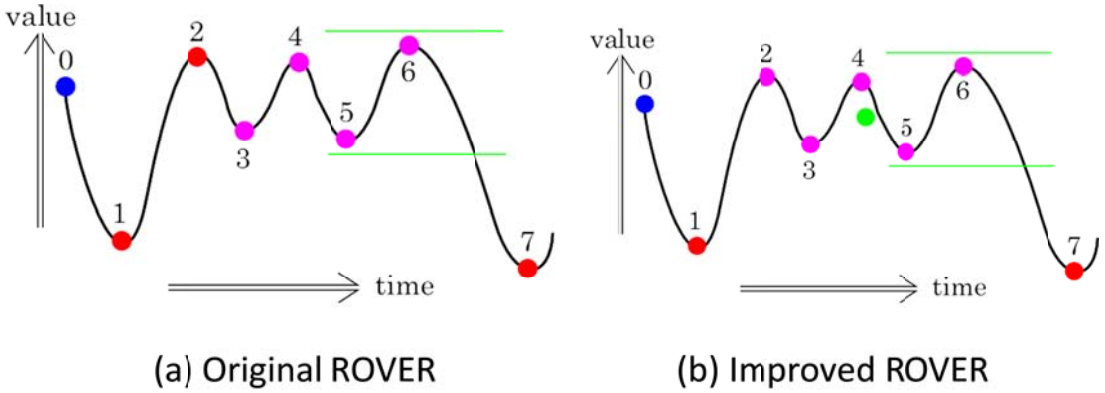

(a) Original ROVER (b) Improved ROVER

Figure 4: Differences between the original and improved ROVER. Time traces of a sample value for peak selection. Red dots indicate the candidate peak value. Pink dots indicate the discarded candidate points. Green lines show the PST boundaries. a) Original ROVER detection b) TUD detection adaptation, which shows the ‘averaged’ consecutive discarded candidates with a green dot.

A further improvement to average peaking was introduced in TUD ROVER algorithm as shown in Figure 5. The improvement consists of performing the averaging of the stick input in the time interval until the body maximum or minimum is experienced. Therefore, the detection is carried to earlier stage of the PST limited interval detected peaks, as presented in Figure 5 by the green dot (improved average peak) showing an earlier detection than the claret red dot (original proposed average peak) and relating the peak of the pilot control to the corresponding body response. This improvement increases the efficiency of the adapted TUD ROVER algorithm in means of peak selection.

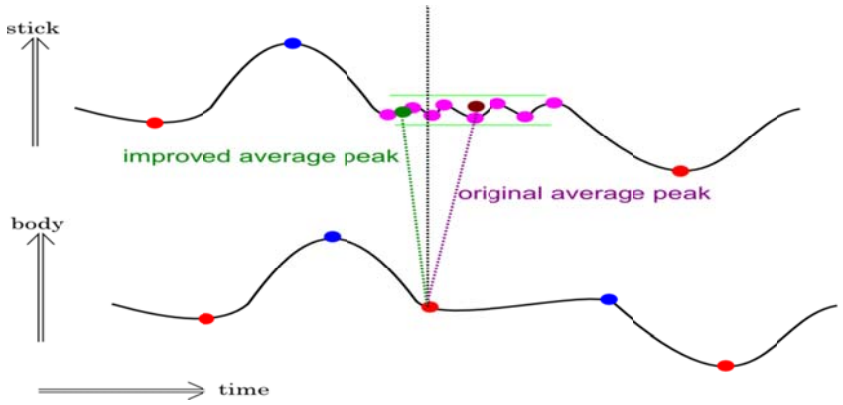

Figure 5: Peak averaging methods in ROVER algorithm.

Example of ROVER Algorithm- Frequency Sweep Input

To check the ROVER algorithm, some simple offline simulations were performed using a frequency sweep for stick from 1 to 8 rad/s at 60 knots for the lateral axis. The lateral stick and roll rate were fed to ROVER and the tests were repeated for the time delays of 100, 200 and 300 ms. In Figure 6 an example of the ROVER output is presented for the frequency sweep with a 300 ms time delay. The first (upper) subfigure shows the stick and body motion after application of the Butterworth filter. The second subfigure (middle) shows when the threshold value for stick amplitude, roll amplitude phase delay or frequency is met. If they are met, a flag is issued. The last subfigure (down) indicates the total ROVER score which is the total number of flags at each time. A score of four indicates a RPC detected (RO4) and a score of 3.5 indicates danger of RPC about to happen (RO3.5).

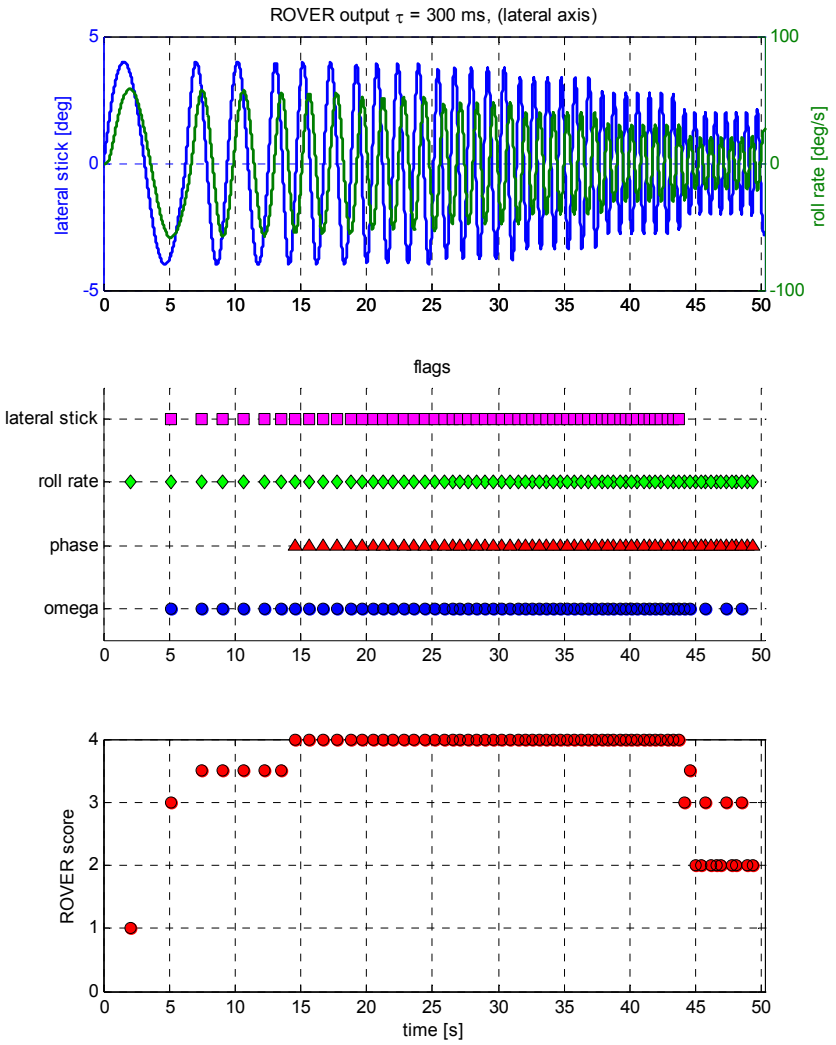

Figure 6: ROVER output for roll tracking at 60 knots with 300 ms time delay.

Table 2 shows the output of the ROVER at 60 kts for the frequency sweep. It can be concluded that indeed, when degrading the HQ of the rotorcraft by introducing a time delay, the number of RPC detected warnings increases with increasing time delay. In general the number of warnings for RPC danger reduces with degrading HQ. Therefore, for degraded HQs a dangerous oscillation of the rotorcraft develops faster into a RPC event than for a helicopter with better HQ.

Table 2: number of ROVER warnings for 50 seconds duration frequency sweep for 1 to 8 rad/s for roll axis at 60 kts

τ [ms]	*RO4*	*RO3.5*
0	0	54
100	26	28
200	43	11
300	48	6

Example of ROVER Algorithm- TUD SIMONA Simulator Results

Examples of the simulator results for two different pilots for the 300 ms time delay case are found in Figure 7 and Figure 8. The first two columns of Table 3 and Table 4 display the complete results for all roll tracking trials for two pilots.

As in the frequency sweep cases the number of RPC detections increase with increasing time delay.

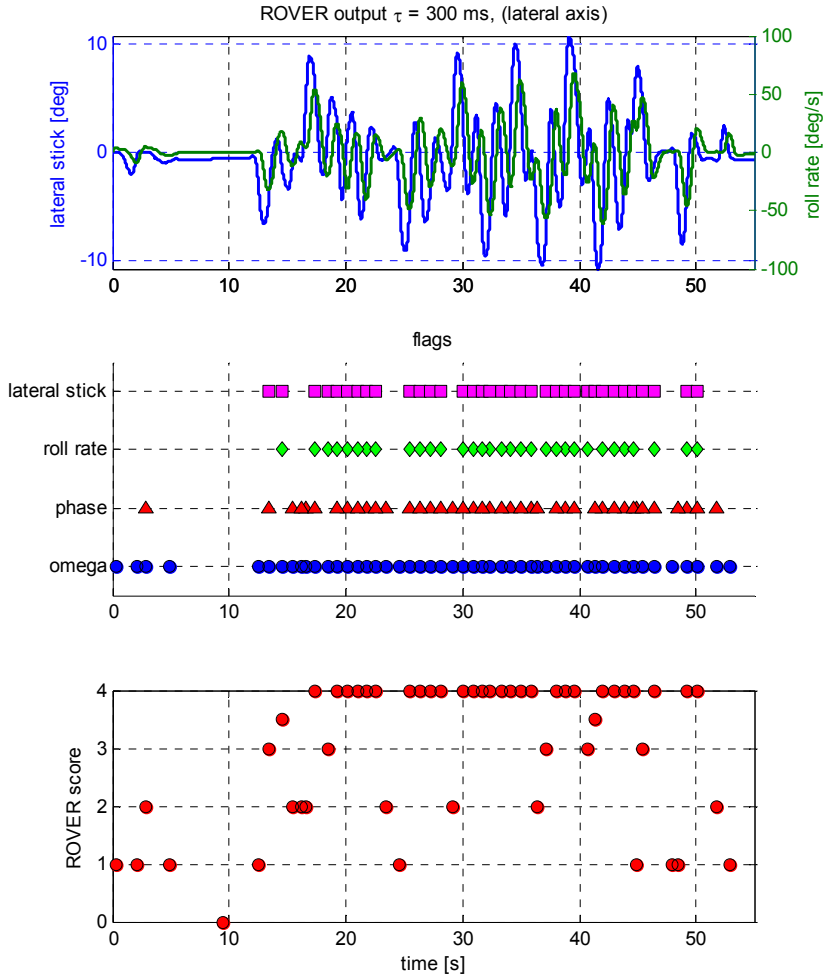

Figure 7: ROVER output for roll tracking at 60 kts with 300 ms time delay in simulator. Pilot 1.

Table 3: Pilot 1 number of ROVER alerts, Handling Qualities Rating (HQR) and Pilot-Induced Oscillation Rating (PIOR)

τ [ms]	*RO4*	*RO3.5*	*HQR*	*PIOR*
0	0	10	4	1
100	1	9	7	1
200	10	8	7	4
300	28	2	7	3

Table 3 and Table 4 present the HQR and PIOR awarded by the pilots. It is interesting to note that Pilot 2 did not report any noticeable RPC during the roll tracking simulator experiments. By close inspection to the stick input and roll rate output temporal behaviour

(Figure 7 and Figure 8) it is noted that there are less oscillations in the traces of Pilot 2 with large time delay configurations.

This could be an indication that, when compared to Pilot 1, Pilot 2, is more able to control a helicopter with degrading HQ and that he possibly unintentionally changed his control strategy to keep the rotorcraft within its performance envelope. Though, he might not be aware of the degradation of the HQ because of the excessive time delay. This could lead to a dangerous situation as RPC events are likely to occur at DHQ levels.

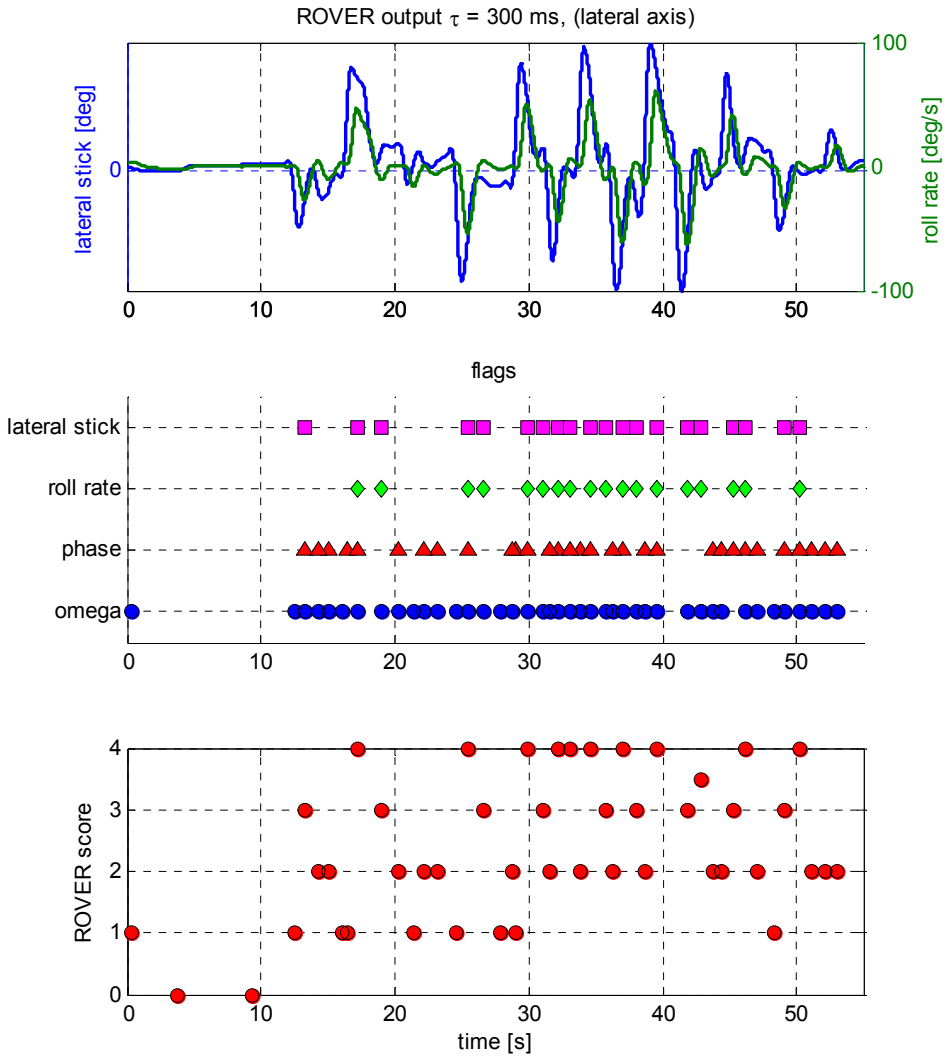

Figure 8: ROVER output for roll tracking at 60 knots with 300 ms time delay in simulator. Pilot 2.

Table 4: Pilot 2 ROVER alerts, HQR and PIOR

τ [ms]	*RO4*	*RO3.5*	*HQR*	*PIOR*
0	-	-	-	-
100	2	8	3	2
200	8	1	4	2
300	10	1	4	2

Combining ROVER Algorithm with Bandwidth Phase Delay HQ assessment

In addition to peak selection updates on ROVER, TUD combined ROVER to the Handling Qualities (HQ) assessment of ADS-33. The scope of the integration of HQ into ROVER detection is to improve the pilot awareness due to incipience of a possible RPC by providing additional HQ degradation warning. Bandwidth Phase Delay (BPD) criterion of ADS-33 was chosen to provide the HQ information. Briefly, this criterion checks the pilot control activity with the corresponding rotorcraft response and provides the level of HQ depending on the bandwidth and the resultant phase of the pilot control-vehicle system. Since ROVER explicitly checks for pilot control activity and the phase between control input and the body angular rate output, ROVER was adjusted to provide detection points superimposed on the BPD determination graph.

An example of this coupling of ROVER to BDP criterion is given below. Figure 9 shows the ADS-33E HQR based on the bandwidth frequency and phase delay for the roll tracking task at 60 kts. It was found that for the roll tracking task, the degradation was from Level 1 at 0ms time delay down to Level 3 at 300 ms. From this figure it is proven that the HQ are degraded by introducing a time delay. Further, it is noted that although the HQ are degraded, there is no indication of RPC proneness based on the ADS-33E guideline. The BPD criterion was applied to the roll tracking test performed at 60 kts in SIMONA simulator.
Figure 10 and Figure 11 present the results for the Pilot1 and respectively Pilot2 as plotted in the BPD map.

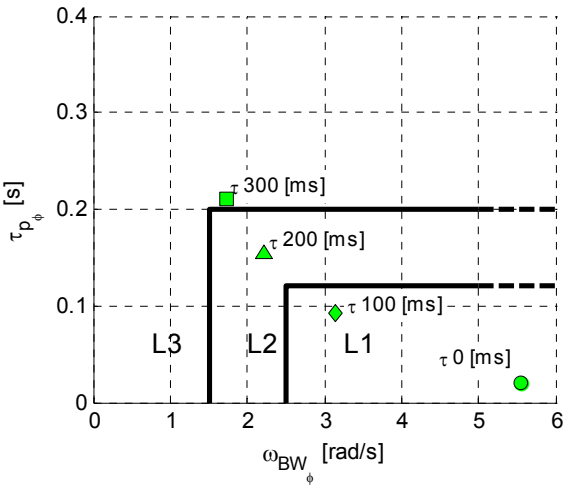

Figure 9: ADS-33E HQ levels for simulation model.

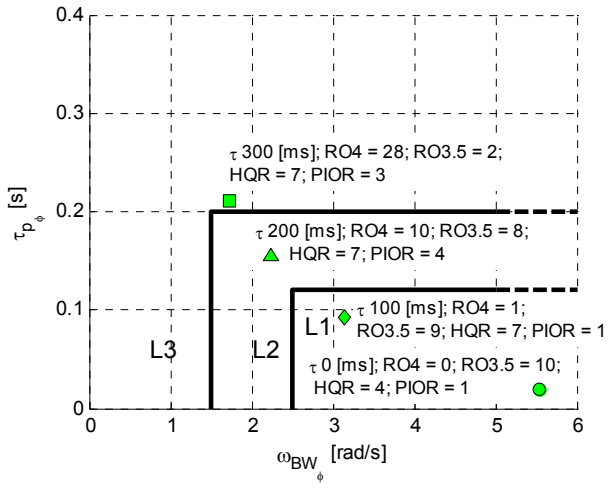

Figure 10: ADS-33E HQ levels for simulation run of pilot 1; number of 4 flags issued by ROVER and number of 3.5 flags issued by ROVER; HQR and PIOR.

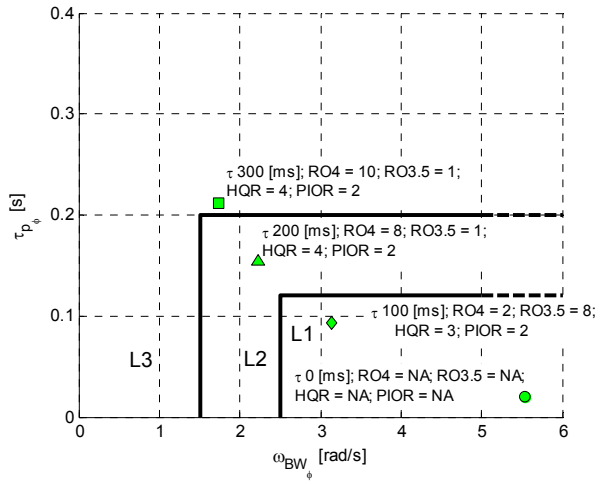

Figure 11: ADS-33E HQ levels for simulation run of pilot 2; number of 4 flags issued by ROVER and number of 3.5 flags issued by ROVER; HQR and PIOR; (green = no RPC prone; red = RPC prone).

To improve the ROVER algorithm with HQ degradation detection, the following method is applied: Alongside ROVER's classical output, the ROVER algorithm is extended to generate the stick frequency. The ROVER score at each instant together with the phase delay are sorted with corresponding stick frequency. Using these data scatter points from the output of the ROVER can be superimposed on the phase diagram of the Bode plot from the simulation model. If the scatter points deviate from the original Bode plot, the HQ may been degraded or improved. This occurs for example when introducing a time delay. The ROVER scatter superimposed on the Bode plot is presented for both pilots in Figure 12 and Figure 13. The RPC detected events are indicated on the Bode plot in yellow colour.

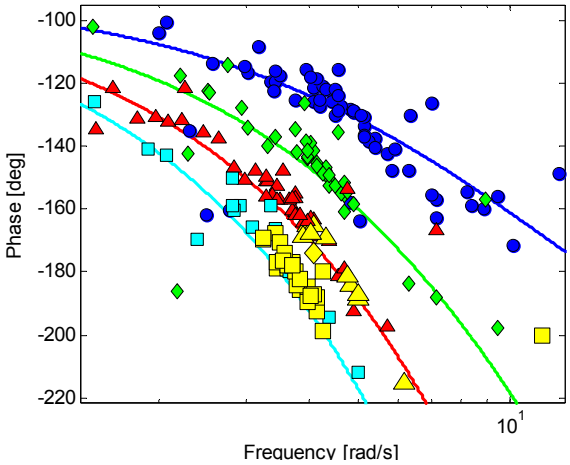

Figure 12: Zoomed phase Bode plot with superimposed ROVER output for pilot 1. Simulation model phase plot: blue = no time delay; green = 100 ms time delay; red = 200 ms time delay, turquoise = 300 ms time delay. Coloured points are corresponding ROVER output. Yellow markers are corresponding RPC detected points by ROVER.

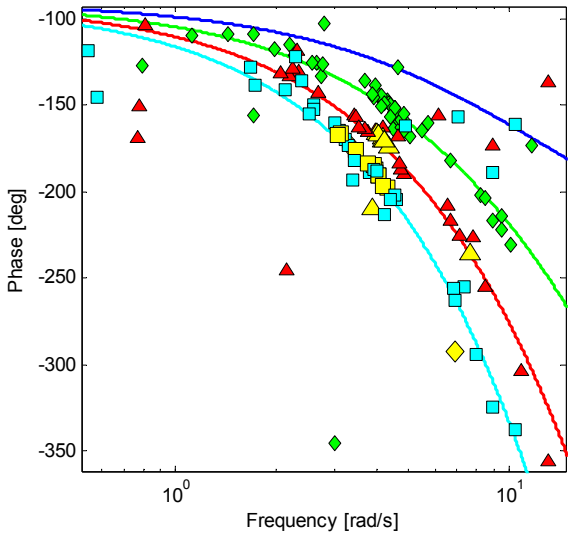

Figure 13: Zoomed phase Bode plot with superimposed ROVER output for pilot 2. . Simulation model phase plot: blue = no time delay; green = 100 ms time delay; red = 200 ms time delay, turquoise = 300 ms time delay. Coloured points are corresponding ROVER output. Yellow markers are corresponding RPC detected points by ROVER.

From Figure 12 and Figure 13 it is observed that in general, when the time delay is increased or decreased the ROVER scatter points are mainly matching the corresponding phase graph on the Bode plot. Therefore, degradation in HQ can be detected in quasi real-time if the algorithm is applied on streaming data.

Another observation is that the majority of the detected RPC (4 flags, yellow markers) frequencies are more or less around the crossover frequencies of the pilot (180 degrees) for the controlled vehicle dynamics. Hence, considering the same amount of pilot control input, possible RPC zones are situated around the crossover frequencies showing that neither the high frequency pilot activity nor the low frequency pilot compensation are the only factors responsible for RPCs. This observation also agrees with the results of Mitchell [17]. Pilot 2

gives only a PIOR of 2 at level 3 HQ. Further, he does not experience the degradation of HQ to level 3 as seen in Figure 11. Contrary, Pilot 1 gives high rating for RPC which matches the output in Figure 12. In order to alert Pilot 2 of the fact that the HQ were degraded when flying with a time delay of 300 ms, the enhanced ROVER can inform the pilot about this HQ degradation. Thus, even if the pilot experiences that the rotorcraft behaves as Level 1 or Level 2 HQ, the improved ROVER would warn him that his actual HQ level has degraded and that the chance of a RPC event has increased. Thus, pilots can prepare themselves for a possible upcoming RPC, or a loss of control scenario (often caused by deficiencies in HQ).

2.2 Prediction using the Phase-Aggression Criterion

Jones et al. [11] proposed a new real-time detection for PIO, the so-called Phase Aggression Criterion (PAC). PAC achieves a 'detection' of an A/RPC through the observation of the Pilot-Vehicle System (PVS) phase distortion and the pilot input rate. Observing pilot input allows one to check that the pilot is coupled with the oscillations (a pre-requisite for PIO) whilst the phase difference allows one to see whether the commanded input is in-phase with the vehicle response. The combination of the two parameters at a finite point in time allows one to objectively assess whether an A/RPC has materialised. The original parameter calculation, formulation of the algorithm and initial piloted simulation results are presented in ref. [11].

PAC was originally developed for observation of Category II PIO (due to quasi-linear system elements). Two test pilots completed a number of pitch tracking manoeuvres, awarding subjective opinion ratings. These subjective ratings, along with pilot comments and objective measures, were used to determine PIO susceptibility boundaries. These boundaries were then used to show at what stage pilots entered ‘Moderate’ and ‘Severe’ PIO conditions during the completed run. Comparison between ROVER was conducted throughout the investigation. Figure 14 shows a result from ref. [11]. This shows identified points determined using the PAC algorithm, for a completion of the pitch tracking manoeuvre. As shown in this case, clearly the vehicle has experienced resultant oscillations. PAC identifies these prior to the largest oscillations. Here, the result could be used to apply alleviation measures, to avoid the divergent PIO seen.

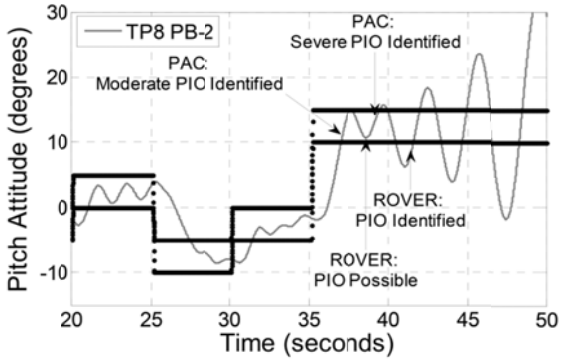

Figure 14: Example of PAC detection for a completion of the Pitch Tracking task.

Based on results observed through the use of PAC, it has been proposed that it can also be used as a prediction algorithm (PRE-PAC). Rather than using a piloted simulation, a simple model of a sinusoidal input is defined. This is based on the important assumption that sinusoidal waves at maximum possible input amplitude with respect to frequency will be encountered by a pilot at some point. Therefore, rather than a sophisticated pilot model, the sinusoidal frequencies show what a pilot 'could' do. In order to use PRE-PAC one needs first

to pre-define input signals to be fed into a simulation model. These have been designed to account for a range of active pilot control inputs. Then, one needs to determine the time dependent 'Phase' and 'Aggression' parameters for each input signal, by running a simulation in the time domain. These results are then used to determine the systems incipience to RPC. The incipience is based on defined severity boundaries, which have previously been determined through a number of piloted simulation campaigns. These boundaries are presented on the Phase-Aggression chart, with some examples shown in Figure 15 to Figure 17. These examples show results from three linear vehicle roll models, for a rate command system. The shaded region represents the region of 'possible' pilot control, accounting for the range of control input frequencies applicable to PIO research (1-10 rad/s). For a given control input signal, one can determine the frequency dependent Phase and Aggression parameters. Moreover, one can determine whether these points are within the 'No PIO' region, 'Moderate PIO' region, or 'Severe PIO' region. Figure 15 shows a PIO robust roll model. Here, for all pilot control frequencies, results are within the 'No PIO' region. Figure 16 shows results from a model found to be incipient to 'Moderate' PIO. Here, the region of pilot control intersects the moderate PIO boundary at approximately 2.5 rad/s. However, a rapid reduction in change-in-phase following 5 rad/s means that the region does not intersect the 'Severe' boundary. Finally, Figure 17 displays results from a PIO prone case, whereby the region of pilot control intersects both the moderate and severe PIO boundaries. Here, the moderate boundary is crossed at 2.2 rad/s, and the Severe boundary at 3.1 rad/s.

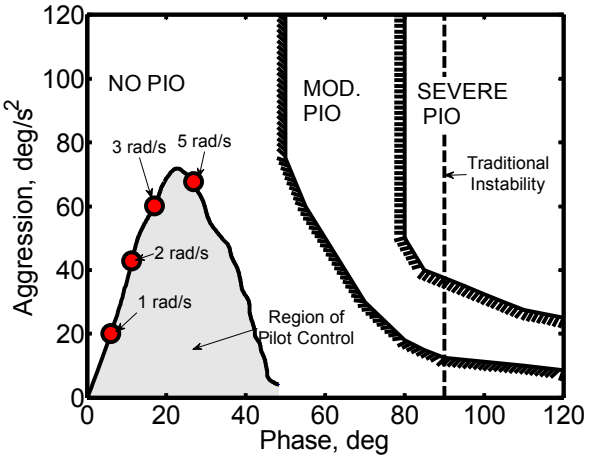

Figure 15: Example of PRE-PAC Results for PIO Robust vehicle model, Lp = 10/s, τ=0ms.

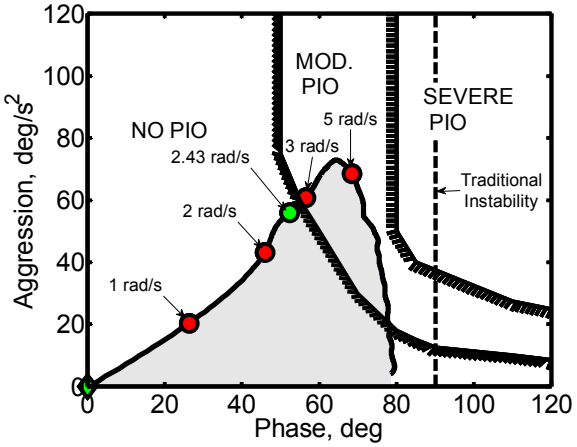

Figure 16: Example of PRE-PAC Results for PIO Incipient vehicle model, Lp = 2/s, τ=0ms.

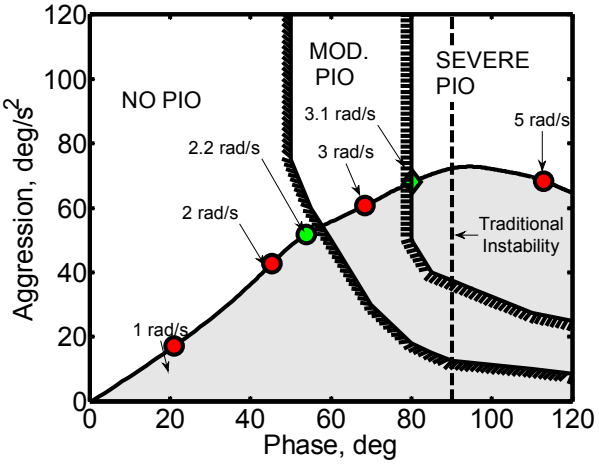

Figure 17: Example of PRE-PAC Results for PIO Prone vehicle model, Lp = 10/s, τ=0.3ms.

To date, boundaries have been constructed to observe the incipience to Category I (linear) PIO for forward flight, roll-axis and for incipience to Category II (quasi-linear PIO) for roll- and pitch- axes.

As defined in Ref. [12], the bandwidth frequency (ω_{BW}) is either the frequency for which the phase has a margin of 45 deg to instability or the point where the gain margin is 6dB greater than the gain required for instability; whichever is the lower frequency. The phase delay, τ_{ps} describes the behavior of the system following initial instability. If there is a rapid change in phase following instability, the phase delay will be large. A large phase delay will force significantly more effort for the pilot, as they must constantly adapt to the sensitive delay.

In this study, the results obtained are compared directly against the boundaries provided in ADS-33E-PRF [12] for target tracking and acquisition (TTA) tasks, for the roll axis in forward flight (airspeed greater than 45 kts). These tasks are those where for the completion of the mission, the pilot must be engaged in high gain closed-loop control. This is the situation where PIOs are most likely to occur. These boundaries have been developed specifically from rotorcraft testing and evaluation. However, they are used to determine predicted HQLs and not PIO susceptibility directly. However, in the presence of transport delays, changes in HQLs give a strong indication of changes in PIO susceptibility. The boundaries used are shown in Figure 18.

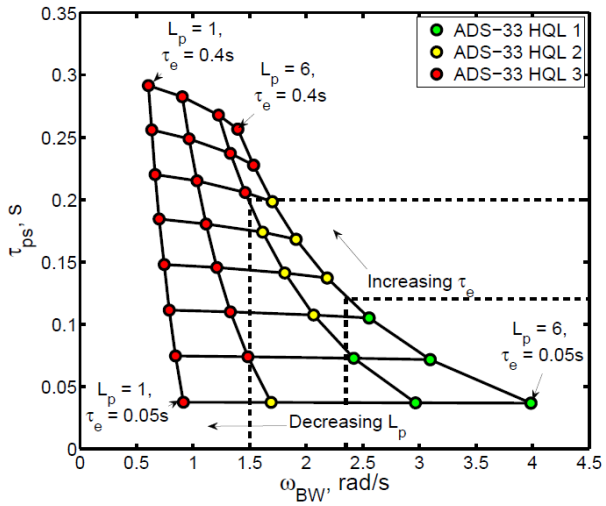

Figure 18: BPD Results for a number of different L_p,$L_{\theta_{1c}}$, and τ values.

In order to determine PIO susceptibility using the BPD criteria, the linear model described in Eqn. (1) was used, varying roll damping (L_p), roll control sensitivity ($L_{\theta_{1c}}$), and vehicle time delay (τ). In Eqn. (1), φ represents the vehicle roll attitude and δ_{1c} represents pilot input at the control stick. $L_{\theta_{1c}}$ was varied in order to conserve a roll rate to control input coupling of 10 deg/s/in. This value was used as it is typical for an agile helicopter. Figure 18 shows the matrix of results obtained, against both ADS-33 boundaries.

$$\frac{\varphi}{\delta_{1c}} = \frac{L_{\theta_{1c}}}{s^2 + L_p s} e^{-\tau s} \tag{1}$$

PRE-PAC has been constructed to give a complete evaluation of the vehicle susceptibility to PIO, with the goal of assessing the control envelope, rather than the point at which instability will occur. Therefore, the primary goal of the criterion is not to directly match predictions made by BPD. However, it is possible to make comparisons based on parameters calculated using PRE-PAC.

The boundaries presented in Figure 18 are focused on the vehicle bandwidth, at a point prior to instability. Essentially, if the pilot applies input signals at a greater frequency than the bandwidth, the system is likely to become unstable. Using PRE-PAC, instead of the `bandwidth' frequency, one can calculate the moderate and severe trigger frequencies ω_{MOD} and ω_{SEV} respectively) to determine the susceptibility. All model configurations shown in Figure 18 were processed using PRE-PAC. This allowed the observation of control envelope incipience to PIO, alongside the trigger frequencies ω_{MOD} and ω_{SEV}. Here, trigger frequencies were determined for the maximum input amplitude. Therefore results show the relationship between maximum pilot control activity and BPD results.

Figures 19 shows ω_{MOD} with respect to ω_{BW}. Also displayed are the HQL predictions determined from ADS-33E-PRF roll-axis target tracking boundaries. Here, there appears to be a strong correlation between the results obtained using these boundaries and PRE-PAC `trigger' frequencies. Predicted HQL regions are clustered, and the results displayed seem logical. Firstly, ω_{MOD} has strong correlation with ω_{BW} for all configurations, with HQL 3 observed for ω_{MOD} less than 2rad/s.

Results in Figure 19 show consistency between PRE-PAC trigger frequencies and ω_{BW}. However, the results obtained using BPD are also reliant upon τ_{ps}. This describes the change in phase at a period past the bandwidth frequency. With results from PRE-PAC analysis, a similar parameter can be defined. If ω_{MOD} is seen as equivalent to ω_{BW} then equation (2) can be used to determine the change in phase $\Delta\omega$ following the initial triggering of a PIO.

$$\Delta\omega \,|_{\omega_{MOD}}^{\omega_{SEV}} = \frac{1}{\omega_{SEV} - \omega_{MOD}} \tag{2}$$

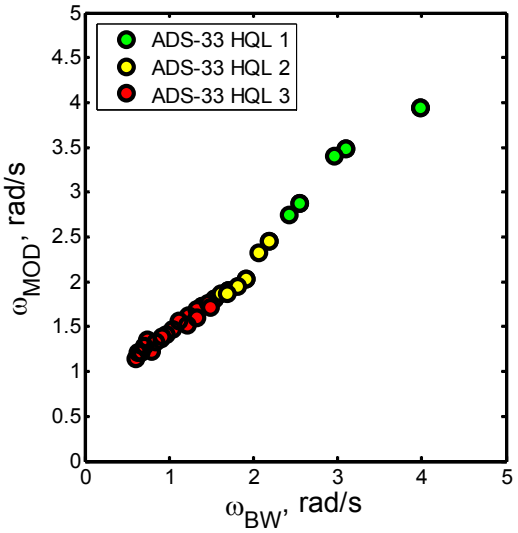

Figure 19: Comparison between moderate cross-over frequency and bandwidth frequency.

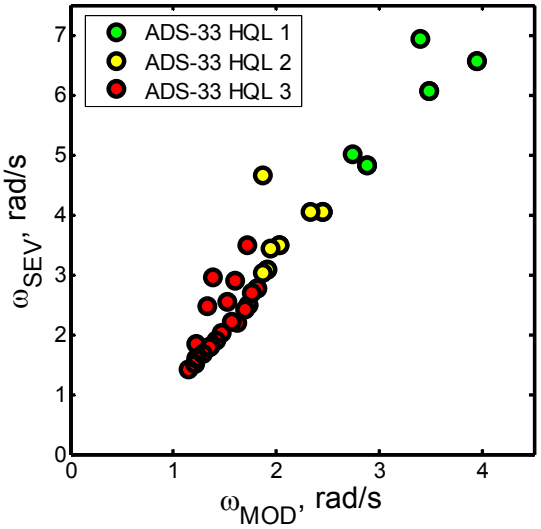

Figure 20: Comparison between moderate and severe cross over frequencies for linear roll models.

Figure 21 shows $\Delta\omega$ with respect to ω_{MOD}. As shown, the figure appears similar to Figure 18, with more emphasis upon the change in frequency. Therefore, for these simple roll-axis models, it appears that results obtained using PRE-PAC can be considered comparable to those obtained using BPD. The correlation for more complex models remains to be seen, but it is hypothesized that correlations shown here will be repeated. These results show that PRE-PAC can offer a similar appraisal to PIO susceptibility as BPD, but also provide additional information, such as conveyed in Figures 15 to 17 to further understand a particular incipience to PIO.

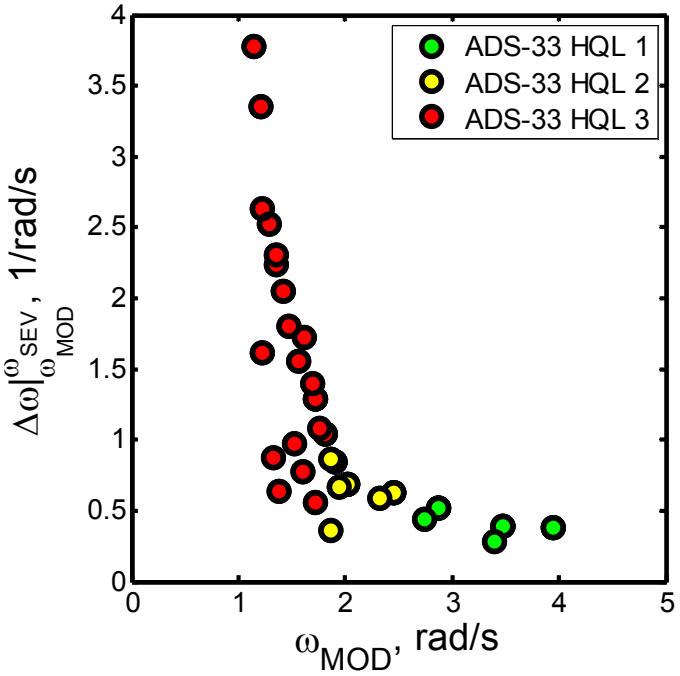

Figure 21: $\Delta\omega$ with respect to ω_{MOD} compared with HQL predictions.

2.3 Prediction based on Boundary Avoidance Tracking

2.3.1 Modelling the Boundary-Avoidance Tracking Process

Gray developed the BAT model, shown in Fig, and provided analysis techniques for estimating the associated boundary-avoidance model parameters [13].

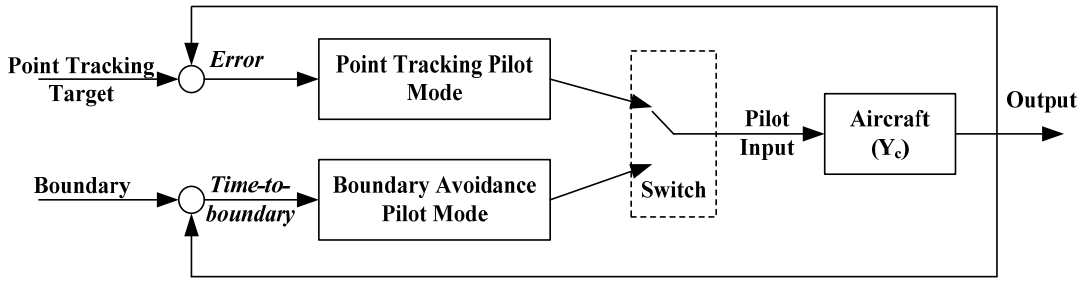

Figure 22: Gray's boundary-avoidance tracking model (based on [13]).

The feedback loop includes both Point Tracking (PT) and Boundary Avoidance (BA) options with a logic switch/selector that assumes no transient; only one of the tracking channels is assumed to be operating at any one time. There are 2 boundaries in this particular model, designated upper and lower and only one can be tracked at a time. A key parameter in the BAT model is the time to boundary (τ_b) in Fig, based on the distance to boundary (x_b) at the current rate of approach ($\dot{x}_b$), defined as follows:

$$\tau_b = \frac{x_b}{\dot{x}_b} \tag{1}$$

This parameter models the pilot's perception of the time-to-contact, introduced by Lee [14] as a development of Gibson's optical flow theory of visual perception [15]. However, it is clear that Gray independently discovered that the time to boundary was a key parameter in the pilot control strategy, without being explicitly aware of τ theory. The BA pilot model in Fig is modeled as a BA feedback gain (K), dependent on the variable τ_b and the relationship is illustrated in Figure 1,

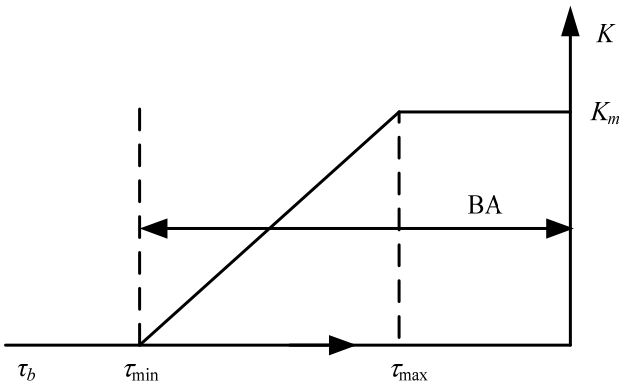

Figure 13: Feedback gain variation with the time to boundary (τ_b).

in which the τ variable is shown in the conventional (negative) sense. The BAT strategy is initiated when τ_b is lower (negatively) than the value $\tau_{\min}$. If the boundary continues to be approached, the feedback gain increases linearly to its maximum, K_m, in the form;

$$K = \frac{\tau_b - \tau_{\min}}{\tau_{\max} - \tau_{\min}} K_m \tag{2}$$

Using Eq.(2), Gray hypothesized that the control increases linearly as the boundary is approached.

The BA pilot activity in Fig. 22 is modeled as a pure BA gain (K) in Eq. (2). While the variation of this gain in Eq. (2) is linear, the essence of this operation is nonlinear, due to the dependence in Eq. (1). This brings with it a difficulty in analyzing the stability of the closed-loop systems in Fig. 22. To address this issue, the BA process is modeled as the following form,

$$K(s) = (\tau_{\min} s + 1) K_b X(s) \tag{3}$$

in which K_b represent the BA control gain. Therefore, the BA feedback part of Gray's pilot model with the nonlinear τ variable can be approximately simplified into a lead perception term. The resultant closed-loop pilot model, including the vestibular and proprioceptive cues is illustrated in Figure .

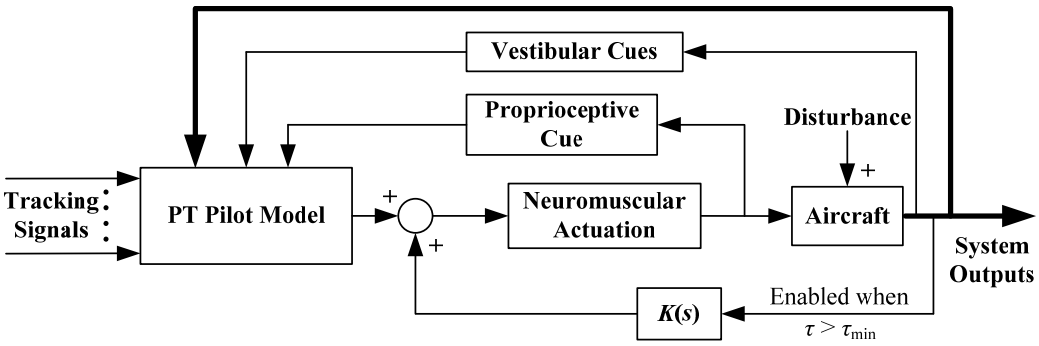

Figure 24: Closed-loop BAT pilot model with the modelled BA pilot part for tracking task.

This rudimentary level of BA description from the derivation process, combined with Figure , shows the essential features in the study of BAT PIOs in this report. First, the effect of the impending boundary is modeled as an additional positive inner feedback to the closed-loop system. This formula, in essence, describes the BA process as a disturbing influence created by the impending boundary, activated at the moment that $\tau > \tau_{min}$, on the primary (outer loop) pursuit task to which the pilot is, until that moment, giving full attention. The positive property of this feedback lies in that, with positive K_b, the resulting control effects will become larger as the detected boundary is approached (larger $X(s)$). Therefore, the stability of the closed-loop system pilot-vehicle dynamics can be changed and the BA process can therefore serve as a PIO trigger. The BAT-PIO onset detection can be estimated by analyzing the effects of the inner linear BA perception-action form on the stability of the outer feedback loop system. Second, the structure in Figure allows the investigation of the continuous contribution of the PT part of the pilot model, even after the BA process is triggered. This is different from previous work, which assumes that the PT and BA work independently, which does not reflect real pilot control activity in Fig. Overall then, the new structure appears to be an appropriate means to describe the pilot dynamics during the BAT process.

2.3.2 BAT Prediction

The 3DOF longitudinal BO105 model linearized from the non-linear BO105 model [16] at 80 kts has been used for the investigation. The model is described as follows,

$$\dot{\boldsymbol{x}}(t) = \mathbf{A}\boldsymbol{x}(t) + \mathbf{B}\delta_{lon} \tag{4}$$

in which $\boldsymbol{x} = \begin{bmatrix} u & w & q & \theta \end{bmatrix}$. The variable *u* is the *x* body axis velocity, *w* is the *z* body axis velocity, *q* is the pitch rate, and *θ* is the pitch attitude. The matrices A and B have the following values:

$$\mathbf{A} = \begin{bmatrix} -0.0397 & -0.0012 & 5.9132 & -28.9264 \\ -0.0149 & -0.8543 & 140.9837 & 10.7268 \\ 0.0082 & 0.0318 & -5.5064 & -4.0324 \\ 0 & 0 & 0.9997 & 0 \end{bmatrix}$$

$$\mathbf{B} = \begin{bmatrix} -1.0278 \\ -3.2261 \\ 1.2680 \\ 0 \end{bmatrix} \tag{5}$$

The neuromuscular damping ratio (ζ_{nm}) and natural frequency (ω_{nm}) in Figure are selected as typical values of 0.707 and 10 rad/s, respectively [17, 18]. The actuator for the longitudinal control input is selected as [17]:

$$G_{\mathrm{ACT}} = \frac{20^2}{(s+20)^2} \tag{6}$$

For the PT pilot model, the model structure used for the investigation is shown in Figure (motion off) and Figure (motion on).

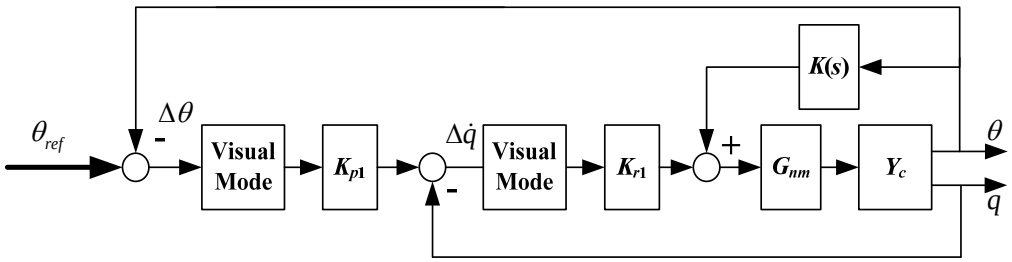

Figure 25: Pilot model for 3DOF pitch tracking task (motion off).

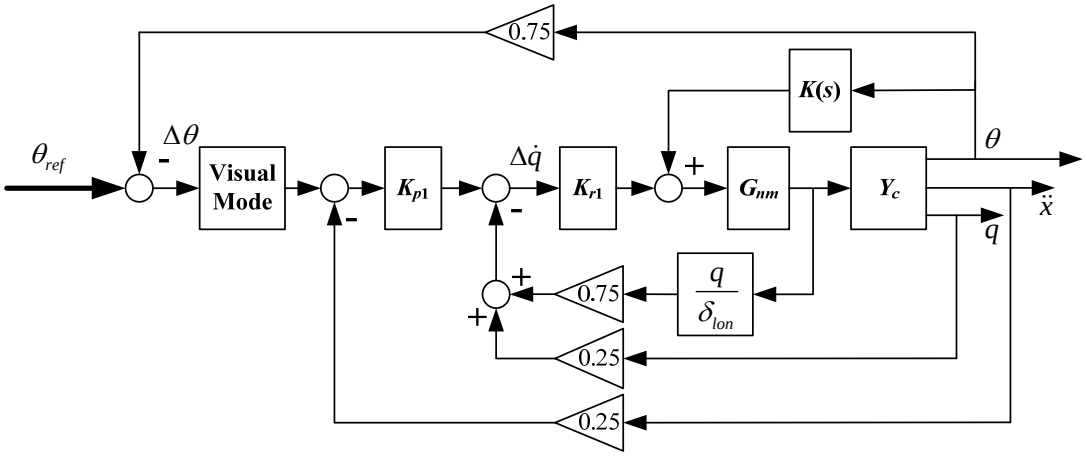

Figure 26: Pilot model for 3DOF model pitch tracking task (motion on).

Here, θ and q are pitch attitude and rate responses to longitudinal stick input (δ_{lon}). The symbol $\ddot{x}$ is the surge acceleration. Compared with the simple form in Figure , the structure of Figure provides more detailed information for pilot modeling. It actually represents a human pilot model that is now able to sense the available vestibular and proprioceptive cues which can be found in Refs [17;18]. The visual model is adopted on each visual channel to reflect the quality of visual information sensed by the pilot [19]. The transfer function in the proprioceptive feedback loop is suggested in Ref. [20] to be the lowest-order model that matches the pitch-rate response with the longitudinal input. Moreover, gain factors with a 0.75/0.25 split in Figure , as described in Ref. [19;20], are used to weight the degree of the importance of each information channel.

With the designed PT pilot, the closed-loop system stability in relation to the BAT phenomenon can now be investigated, subject to the variations of the 3 most interesting parameters: τ_{min}, K_b, and θ_d (boundary size). The smallest critical K_b values (K_{bc}) that bring the closed-loop system (θ_{ref}/θ) to the neutral stability condition, with regard to various τ_{min} values (up to −10s). This is shown in Figure .

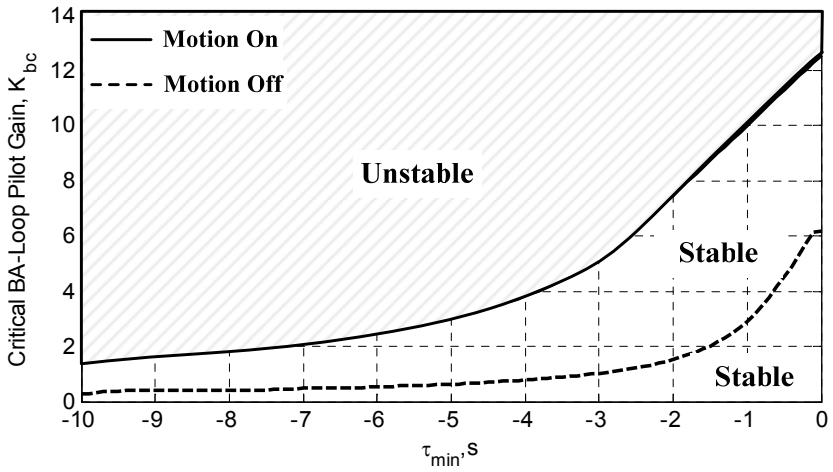

Figure 27: Stability regions with motion on and off against the BA initiation timing τ_{min} .

Figure is obtained with the τ_{min} range (−10, −0.2 s). The selection of this τ_{min} region is based upon the findings of previous research [21;22]. As shown by Figure , both K_{bc} curves have an approximately similar shape, but with a significantly improved stability region for motion on.

Moreover, the stability-separation curves sharply increase as τ_{min} increases. This indicates, perhaps counter-intuitively, that the earlier the pilot initiates the BA process, the lower the level of control margin (the stable range of the gain K_b) will be available. This provides the pilot with less possibility of recovering from the influence of the approaching boundary. The primary reason for K_{bc} reducing as τ_{min} (negatively) increases is due to the fact that this situation requires more pilot control effort to generate a lead equalized visual cue, leaving less control margin available for other tasks. The increased amount of lead requirement actually increases the effective time delay of the pilot-vehicle system [23-25]. Under these situations, pilot performance can be significantly degraded.

The related open-loop ($\Delta\theta/\theta$ in Figure) crossover frequency (ω_c) and the open-loop neutral stability frequency (ω_u) where the open-loop phase angle is -180° with regard to K_b and τ_{min} is plotted in Figure .

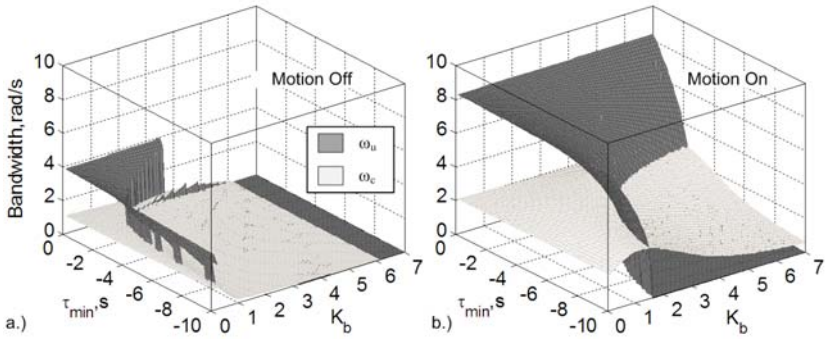

Figure 28: The bandwidth characteristic parameter variation with K_b and τ_{min} .

Two features can be observed in Figure . First, the substantial influence of the inclusion of the BA loop can be immediately observed by the reduction of two bandwidth characteristic parameters, even reaching close to zero, as K_b or τ_{min} (negatively) increases. The second feature, noted from Figure , is that the motion-on pilot-vehicle configuration achieves a superior stability performance, being improved by a factor of around 2. Its ω_c curve surface initiates from 2 rad/s (at the left corner, K_b starting from 0.20), complying with the design objective, and then stays at this value over a large region of the parameter space until crossing the ω_u surface as K_b and τ_{min} vary. This is the opposite to what can be found in Figure *a*, where ω_c initiates from around 1 rad/s, even though it is designed to be 2 rad/s (without the BA loop, K_b = 0). This indicates that with motion on, the introduced BA loop has no significant influence on the pilot control activity (reflected by ω_c) and the consequent closed-loop tracking performance within this region. As K_b and τ_{min} increase, the ω_c surface slowly decreases but ω_u rapidly drops to zero.

The main reason for the stability region and bandwidth differences noted in Figure and Figure is likely to be due to the increased number of cues being available in the latter case (in Figure) i.e. the inclusion of the vestibular and proprioceptive feedback loops. Ref. [24] have found that the availability of these cues can be attributed to a reduction in the effective time delay and thus improved closed-loop stability performance because there is no need to generate angular rate or acceleration information by means of a lead equalized visual cue. The results above have demonstrated that the extra BA effort correlates with a reduction in the open-loop frequency bandwidths (in Figure) and the influence of the BA loop on the closed-loop stability and tracking performance equally increases the effective time delay. Taken together, the inclusion of the vestibular and proprioceptive feedback loops compensate for the penalty imposed by the addition of the BA loop.

The discussion above highlights the significant effects that the BA activity can have on the pilot-vehicle system performance. However, the investigation carried out so far only focuses on the stability of the system, without taking into consideration any boundaries or limits. The key facets of the BAT phenomenon stem directly from operational requirements and are hence mission-specific. Therefore, the results shown in Figure and Figure may be conservative in that the closed-loop system can be stable but its response, depending on the type of input, may violate the boundary that could be considered to be a fatal error in normal flight operations (if the boundary happened to be the ground level, for example) [13]. Therefore, the boundary-constraint condition must now also be included in the investigation.

Figure illustrates an idealized boundary avoidance tracking experiment, the pitch tracking task.

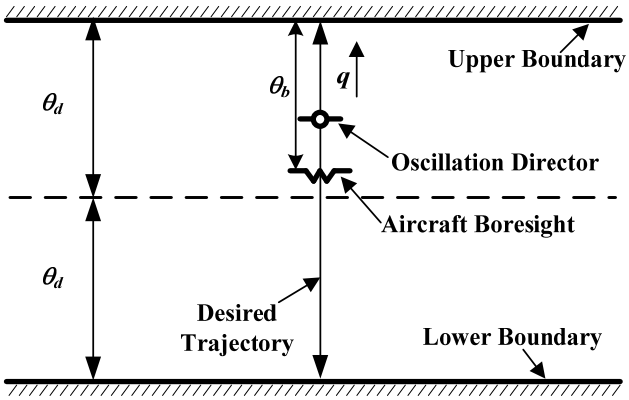

Figure 29: Illustration of a pitch tracking case with the boundary limits.

The pitch tracking task of Figure shows that the pilot (or pilot model) is required to command the aircraft bore sight symbol through the vehicle dynamics to capture a moving target (oscillation director), constrained within 2 boundaries. This is similar to a task flown in a simulation facility for an earlier investigation into rotorcraft pilot couplings, reported in Ref. [26]. For the purposes of this report, the path of the director is composed of four sinusoids as described in Eq. 7,

$$\sin(0.1\pi t)+3\sin(0.05\pi t)+2\sin(0.15\pi t)+3\sin(0.3\pi t) \tag{7}$$

in order to try to reduce the ‘predictability’ of a single sinusoidal signal.

A series of boundary sizes, 6 - 15 deg, with an increment of one degree were selected for the investigation. The lowest boundary size takes the maximum amplitude (6 deg) of the desired combined signal in Eq. (7) into consideration. The fatal and safe regions under these boundary sizes are illustrated in Figure .

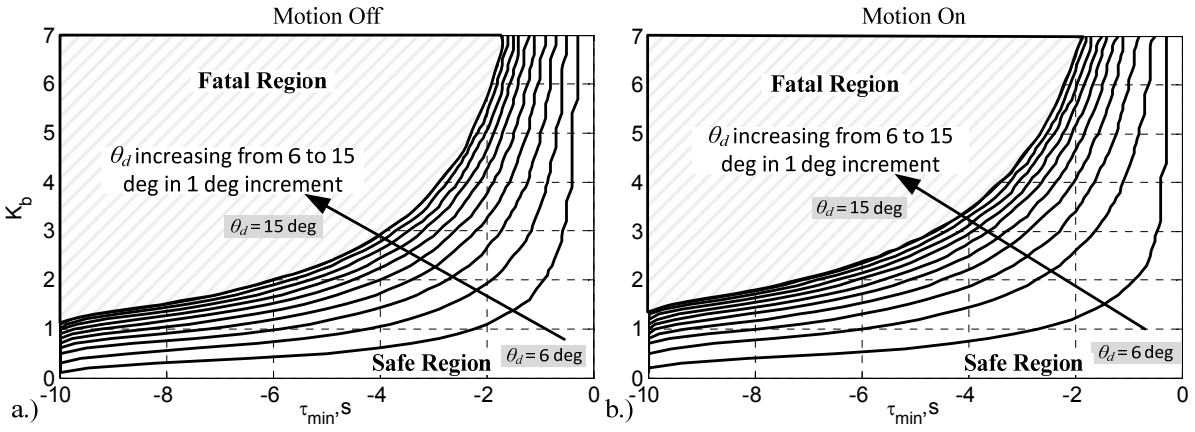

Figure 30: Fatal and safe region variation with boundary size for pitch model analysis.

Figure shows the profound influence of K_b and τ_{min} values on the safe flight region (entering into either system instability or violation of the boundary limit), subject to the various boundary sizes. These figures show that the safe K_b - τ_{min} regions within the designated boundary size become larger as the boundary size increases. This indicates the decreasing influence of the increased boundary size on pilot control activity. Four interesting features can be summarized from Figure . First, for the same τ_{min} value, the larger boundary size allows larger attainable pilot effort (K_b) and gives the pilot more control margin to avoid the impending boundary. This is especially reflected by the smaller τ_{min} values where there is no limitation on the K_b value that can be applied. This is actually a consequence of the BA process not being activated. The designed PT pilot model can ignore the boundary for a given boundary size where the τ_{min} values is relatively small (below a certain threshold). For example, for the designed experimental configuration, the boundary has no influence on the closed-loop tracking task when $\tau_{min} > -1.0$ s in the case of θ_d = 8 deg, as shown in Figure . Moreover, the larger boundary size will result in a larger negative τ_{min} threshold. Second, compared with those in Figure , the proposed stability curve in Figure follows a similar shape, but appears to be too conservative, as expected, especially within the low τ_{min} range. The main reasons have been given above. However, the curve in Figure is still useful because it illustrates the gross degree of the closed-loop system stability associated with the BA process, without requiring the prior knowledge of the desired tracking signal and the boundary size or other mission-specific details. Third, for the same K_b value, the range that the modeled pilot maintains safety will decrease as τ_{min} becomes negatively larger. This is reasonable in that for the same boundary size, the negatively larger τ_{min} means more lead-equalization effort is required. This will increase the effective time delay, as discussed above. Finally, the better closed-loop performance shown in Figure and Figure , compared with each boundary size, is also reflected in the larger safer region in Figure .

With the derived safe region of Figure , the tracking performance for these boundary sizes is predicted in Figure . The tracking performance is defined as the root-mean-squared (RMS) difference between the desired (Ref) and simulated (Sim) pitch attitude responses.

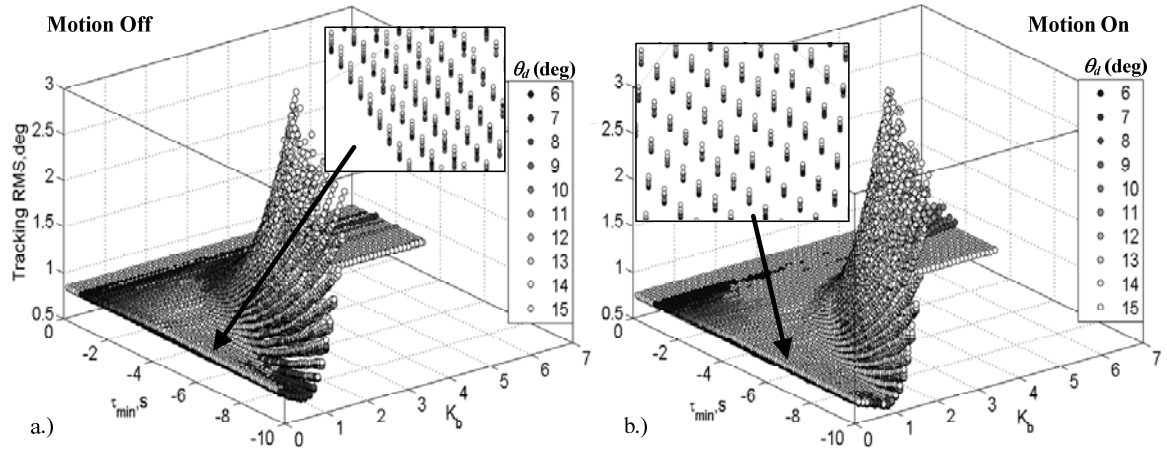

Figure 31: Tracking RMS variation with different K_b and τ_{min} values.

Figure shows the characteristics of the pitch tracking features under the variation of the boundary size. These can be summarized as follows. First, because the positive feedback property of the BA loop has a significant influence on the closed-loop stability in Figure and Figure , it is expected that the larger positive feedback from the inner loop will result in a larger tracking error, arising from the reduced open- and closed-loop bandwidths. The distribution of the tracking RMS performance in Figure confirms this expectation as K_b increases. This finding can be used to explain the phenomenon found in Refs. [21;27;28] for fixed-wing aircraft, whereby the tracking performance slightly improves as the boundary size decreases. Moreover, the previous study has assumed that, for the same task under the same flight condition, a pilot adopts the same τ_{min} value. As shown in Figure , the decreasing boundary size will compel the pilot to adopt a smaller K_b value to maintain safe flight which will in turn have a lesser effect on the outer closed-loop tracking performance. As a consequence, the smaller boundary size can actually increase tracking performance. This phenomenon is also reflected by the points within the region with the lighter shading in Figure (those τ_{min} - K_b pairs in the common safe region in Figure). These points show that tracking performance slightly improves by approximately 5%, illustrated by a sampled zoomed area, as the boundary size decreases.

Second, the smaller boundary size results in a narrower safe region in Figure and a worse tracking performance, shown by the darker region in Figure . Previous studies [21;27;28] also found that the tracking performance degrades when a certain 'critical' boundary size is reached and this can even lead to BAT-PIO situations. This primarily results from the reduced control margin for the smaller boundary size that makes the pilot more susceptible to system safety maintainability problems (i.e. a narrower safer region) as illustrated in Figure . If the boundary size is too narrow, for the same τ_{min} value, a small increase in K_b as the boundary approaches will cause a violation of the safe region.

Third, the two configurations depict a similar RMS-value distribution. However, the RMS values with motion on in Figure *b,* at the base of the distribution curve, are slightly improved by approximately 9% when compared with those of Figure *a*. This is to be expected since the frequency bandwidths associated with ω_c and ω_u of the motion-on configuration in Figure *b* are larger than those in Figure *a*. The larger ω_c values lead to better closed-loop tracking performance.

At the end of this Section, 3 cases with τ_{min} = –2.0 and K_b = 3.0 with boundary sizes of 6, 10, and 15 deg have been selected, taking the tracking performance and closed-loop stability into consideration, to illustrate how the pilot model BA control effort varies with various boundary sizes. The simulation results with motion off and on are presented in Figure and Figure , respectively.

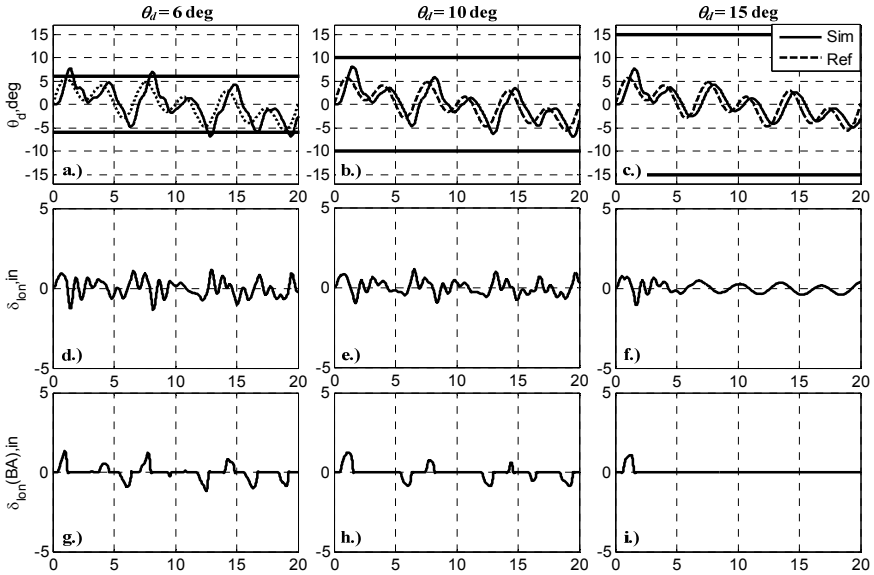

Figure 32: Illustrating boundary effects with normal pilot aggressiveness (motion off, k_{agress} = 1)

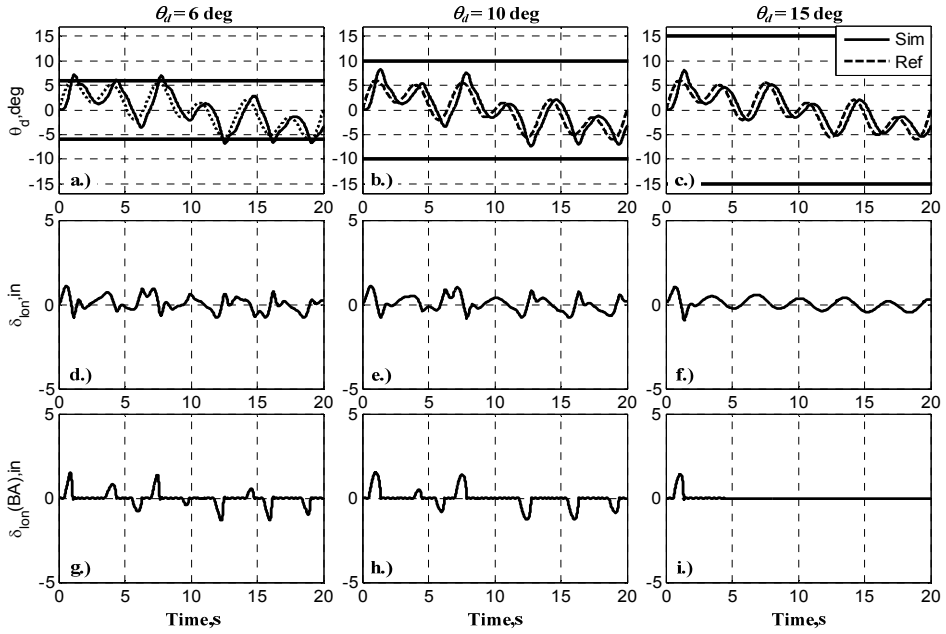

Figure 33: Illustrating boundary effects with normal pilot aggressiveness (motion on, k_{agress} = 1)

Figure and Figure show the significant influence of the impending boundary on the pilot control behavior and the resultant tracking performance. The location of the selected τ_{min} and K_b values in Figure , for both configurations, predict that the case with θ_d = 6 deg will result in a failure situation (i.e. a boundary exceedance) whilst the other 2 cases will be successful. The results here have confirmed by these predictions. For the 6-deg case, the tight boundary results in pitch oscillations within the regions close to the boundary that are then quickly damped when the maneuver returns within the boundaries. This is consistent with Gray's model in Eq. (2) in that the BA process is excited only until τ_{min} is larger than a threshold value. Moreover, the observed decreasing influence of the BA on the outer-loop control

activities when far from the boundary, analogously models the normally recommended strategy to address PIO situations i.e. to back out of the control loop [29]. Finally, the impending boundary introduces extra pulse-like pilot BA control effects and these further result in the severe variations in the pilot's longitudinal stick control (δ_{lon}). As the boundary size progressively increases, Figure also shows that the resultant influence becomes significantly weaker (θ_d = 10 deg) and then quickly disappears after experiencing an initial influence (θ_d = 15 deg). In addition to these similar results, the comparisons between Figure and Figure indicate that, for this tracking task, the motion and proprioceptive cues available have resulted in better tracking performance and less pilot control activity, in good agreement with the larger ω_c bandwidth in Figure .

2.3.3 BAT Pilot Model Investigation Using Piloted Simulation

Based upon the results of the modeling and simulation exercise above, a number of predictions can be made about the way that a pilot might be expected to behave when confronted with a point tracking task that becomes a boundary avoidance type task either in flight or, more particularly, in a simulation environment. First, it would be expected that there would be a difference in both the observed control behavior and tracking performance between test points with any motion cueing system switched on and switched off (or no motion cueing system available). Furthermore, the tracking performance with motion off is likely to be more inconsistent between test points than with motion cueing on (based upon the sharp roll off of bandwidth in Figure). Second, it would be expected that tracking performance would vary with the size of the time to go to any boundary to be avoided. The variation may be better or worse with, say, decreasing boundary size, but this is dependent on both pilot gain and the moment that the pilot responds to the boundary itself (see Figure). Finally, the modeling exercise indicates that BAT PIOs will be difficult to initiate but that they should be easier to trigger with any available motion cueing off. Figure shows some high BA control gains required for instability to occur but that the required bandwidths would be lower, and closer to typical achievable pilot values for motion off cases. Once a BAT PIO is initiated however, it should occur around the frequency ω_u. In order to test these predictions, a simulation experiment was conducted. This Section reports on that experiment and compares its findings with the theoretical study reported thus far.

A. Experimental Set-Up

The experimental study was conducted using the HELIFLIGHT-R simulator at The University of Liverpool [18]. The external and interior views of the simulator are shown in Figure .

Figure 34: The external and interior views of HFR [30].

The proposed closed-loop BAT model of Figure was configured to represent the task conducted in the HELIFLIGHT-R simulator as shown in Figure .

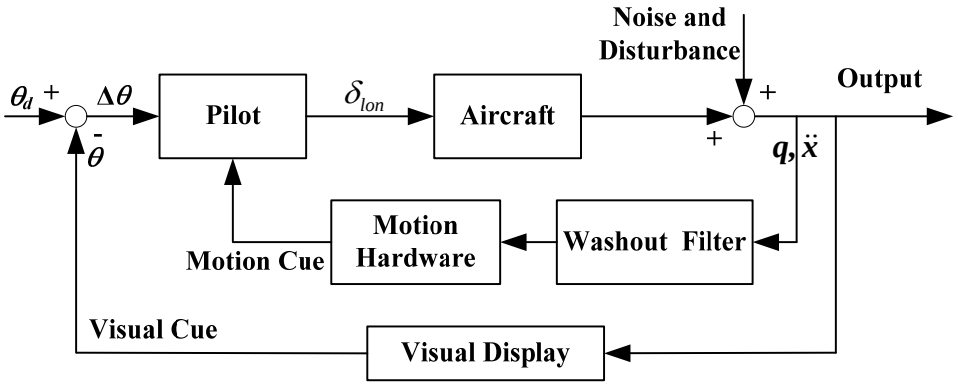

Figure 35: Diagram of pilot-in-the-loop simulation in the HELIFLIGHT-R simulator.

The following should be noted in relation to Figure . First, the same aircraft model and pitch tracking task as for those used for theoretical analysis in Section IV were implemented. Therefore, during the simulation process, only the longitudinal control channel was available to the pilot, the other three (lateral, collective, yaw pedals) had no influence on the model response. Because of the available vertical field-of-view in the HELIFLIGHT-R simulator, the maximum boundary size used for the experiment was 12 deg, as opposed to the 15 deg used for the theoretical investigation. Second, for the motion-on configuration test points (consisting of the motion system hardware and washout filters illustrated in Figure), only the surge acceleration ($\ddot{x}$) and the pitch rate (q) were fed to the motion base drive algorithms. This is consistent with Figure . Finally, the pilots were instructed to focus on the head-up display (Figure) that showed the tracking task symbology and to ignore the head-down display panel during the task. The external visual environment was severely degraded by a simulated visual representation of a thick fog. This minimized the possibility of the pilot being distracted by other objects in the visual scene. All of these measures were undertaken to try to ensure that the only visual cue available to the pilot was the pitch attitude difference ($\Delta\theta$).

Two experienced pilot subjects (A and B) participated in the experiment. Pilot A is a current fixed-wing commercial airline pilot, a former Royal Navy rotary-wing pilot and is a graduate of the Empire Test Pilot School. Pilot B is a current military rotary-wing test pilot.

B. Experimental Results

The simulation results are summarized in Figure and Figure . In these figures, the cutoff frequency (ω_{cut}) is adopted to measure the frequency of pilot control activity applied [31].

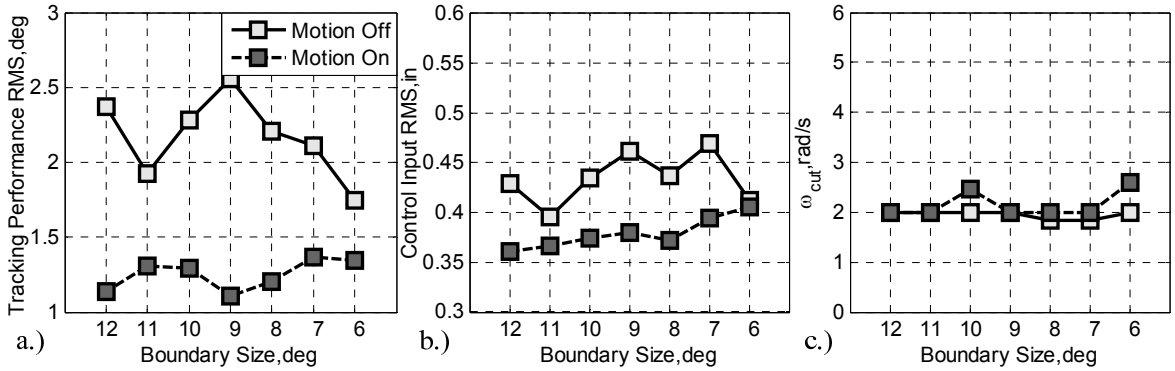

Figure 36: Illustration of tracking performance and control activities for Pilot A.

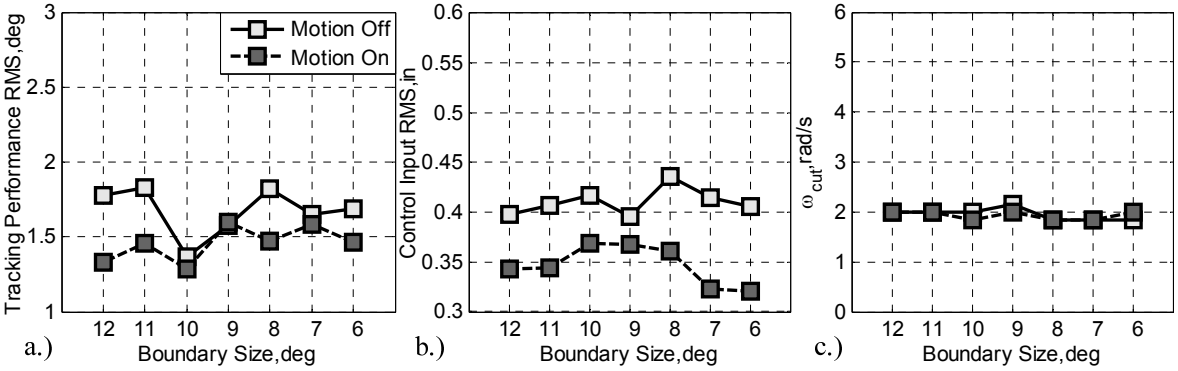

Figure 37: Illustration of tracking performance and control activities for Pilot B.

Figure and Figure can be used to compare the results of the simulation experiment with the predictions made earlier in the Section. In accordance with those predictions, Figure *a* and Figure *a* show a different tracking performance between the motion-on and –off cases for both pilots. In general, the observed motion-off tracking performance is worse (larger RMS values) than the motion-on tracking performance. These findings are consistent with the theoretical analysis of Section 2.3.2 whereby the inclusion of the vestibular and proprioceptive feedback loops/cues reduces the effective time delay in the pilot-vehicle system, thus increasing the closed-loop performance.

Figure *b* and Figure *b*, in agreement with the predicted behavior trend, show different control activity (in terms of different control input sizes) from both pilots. Figure can be used to help explain these observations. First, using the methodology based on optical τ information [30], the average τ_{min} values were found to be: −1.4 s (Pilot A) and −1.2 (Pilot B) for motion off, and −1.1 s (Pilot A) and −1.1 (Pilot B) for motion off. These τ_{min} values, as well as the degraded (generally) tracking performance as boundary size decreases (motion on), indicates that the related (τ_{min}, K_b) pairs are located within the inner-left (darker shaded) regions of Figure . Meanwhile, for motion on, the small control input variation shown in Figure *b* and Figure *b* indicates only a small variation in K_b values. Combined with the wider bandwidth in Figure and the larger stable region in Figure , this would lead to the observed small variation in control input with motion on, and similarly the larger variation with motion off.

Although the trends indicated above are consistent with the model predictions, it should be noted that the experimental tracking RMS values achieved (1.3 – 2.5 deg) are nearly twice as large as the related theoretical ones (< 1 deg) based upon their posited location in Figure . The differences can mainly be accounted for as follows. First, there is a time delay in the HELIFLIGHT-R simulator due to filters, actuator dynamics, and digital system delays that

contribute an incremental time delay of approximately 125 ms between inceptor input and cue initiation. This time delay value was not included in the original theoretical analysis (Figure and Figure) but it can have a significant influence on the closed-loop performance, such as reducing ω_c and deteriorating the tracking performance. The former effect is evident in Figure (for motion off), where the analysis has been re-run with a time delay of 200 ms. By comparing this Figure with Figure , it is apparent, particularly at low τ_{min} and K_b values, that there is the expected reduction in system bandwidth.

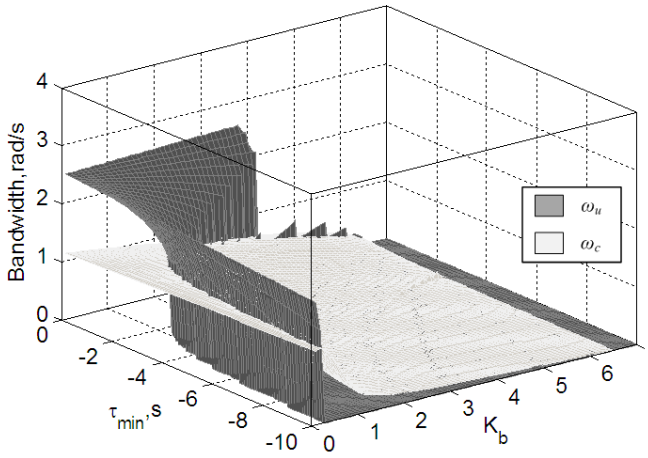

Figure 38: Bandwidth variation with time delay (200 ms, motion off).

Figure shows the effect on the analysis that resulted in Figure with the time delay included. It is now evident that the predicted error is more consistent with that observed in the experiment (again, in the left-hand darker shaded region), albeit at the upper end of the observations.

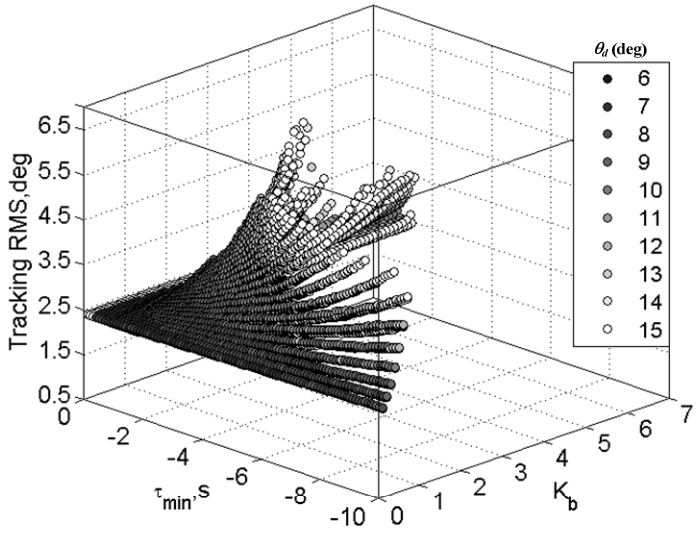

Figure 39: Tracking RMS variation with different K_b and τ_{min} values with time delay (200 ms, motion off).

It was also posited above that the tracking performance of a pilot was likely to be more variable with motion-off and more consistent with motion-on. Figure *a* and Figure *a* arguably show that this to be the case, particularly for Pilot A. For the motion-on cases for both pilots, there is an apparent steady trend for a generally worse target tracking performance as the boundary size decreases, but with a variation of much less than 0.5 deg. For pilot A, with motion off, the trend is generally for increased tracking performance with decreasing boundary size but with a variation of around 1 deg. For pilot B, the trend is arguably neutral

with a variation of between 0.5 and 0.75 deg. these results also support the, perhaps unhelpful hypothesis, that tracking performance can both increase and decrease with decreasing boundary size.

Figure *c* and Figure *c* have been included to verify the pilot cut-off frequency assumption in the implemented multi-loop PT pilot model. It can be seen that the cutoff frequency values (ω_{cut}) of both pilots obtained from the experiments generally approach the desired 2 rad/s used to build the PT pilot model. This indicates that the two pilots tended to adopt a similar control bandwidth, but with a different control effort shown, in Figure *b* and Figure *b,* despite the imposed boundary.

The final prediction made using the model was that BAT PIOs would be difficult to trigger but that it would be easier to do so with motion cueing off. This was based upon the fact that to be able to generate a simulated BAT PIO, K_b has had to be increased up to be an "excessive" value (6) and when this was done, ω_u reached a high value of 8 rad/s. It has also been found to be difficult to trigger a BAT PIO experimentally without further reducing the workload margin, defined as the pilot's capacity to accomplish additional tasks [32]. Indeed, for the experimental campaign conducted for this paper, it was also found to be very difficult to trigger a BAT PIO event. In the end, to address this difficulty, a 100 ms transport delay, which is equivalent to increasing the pilot's lead control effort in the PT pilot model, had to be introduced to trigger a BAT PIO. The only BAT-PIO case available from this experiment is illustrated in Figure . It should be noted, that, in line with the predictions, this could only be achieved with the simulator motion cues turned off.

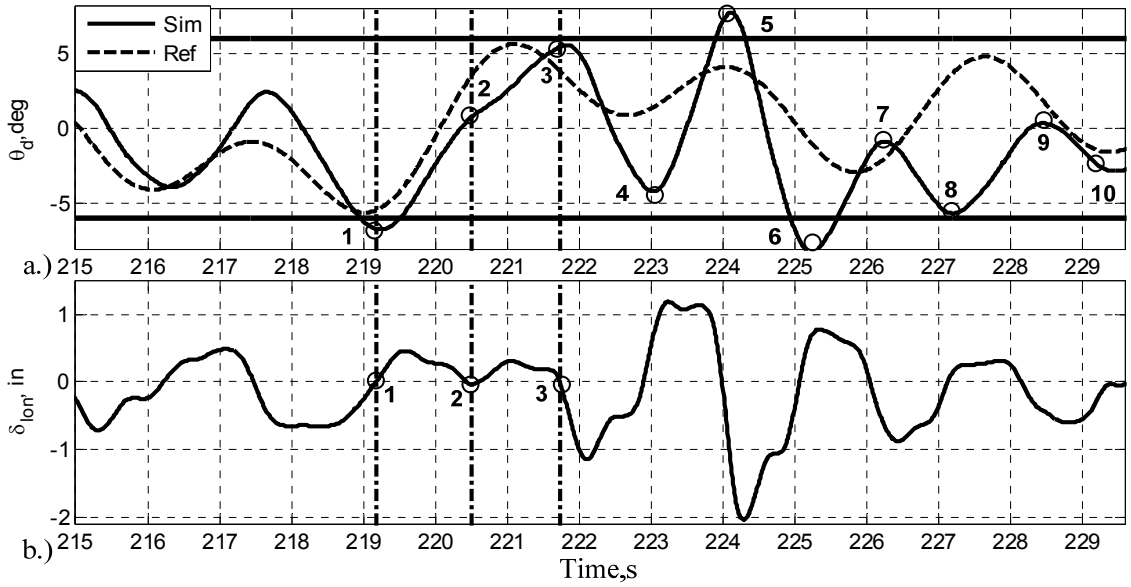

Figure 40: Illustration a BAT PIO with additional 100 ms transport time delay (Pilot A, motion-off).

The short-duration large amplitude oscillatory sequence in Figure has a frequency of 2.7 rad/s. This is close to the theoretically predicted maximum ω_u value of 2.5 rad/s in Figure . Following this event, Pilot A also commented, unprompted, that at or around Point 2 in the manoeuvre, he became aware of the impending upper boundary. At this point, he had to divert part of his attention from the original full PT task to deal with this new situation. This apparent reference to a split between attention on the PT and BAT tasks lends further support the BAT pilot model structure proposed in Figure .

2.4 Prediction based on Optical Tau

The previous research also found that BAT-model parameters could be established using $\dot{\tau}$ and $\ddot{\tau}$. A strong correlation was shown to exist between the lateral control activity and the second-order derivative of tau ($\ddot{\tau}$). The deviations from the assumed $\dot{\tau}$ constant strategy are manifest in variations in $\ddot{\tau}$ for determining the BAT timing parameters, in contrast to the control acceleration variations proposed by others. The values of $\dot{\tau}_b$ and $\ddot{\tau}_b$ (here the subscript *b* means the boundary) at the reference line, defined as the position where the pilot initiates the deceleration phase (e.g. the runway edge in Refs [33;34]), can be used to establish the potential for a BAT event/PIO. The hypothesized conditions are summarized in Figure 41:.

The key result of the first phase of research was therefore to propose Figure 41:, although in a slightly different format, with slightly changed descriptors, as a means of either predicting the onset of or analyzing, after the fact, a BAT situation.

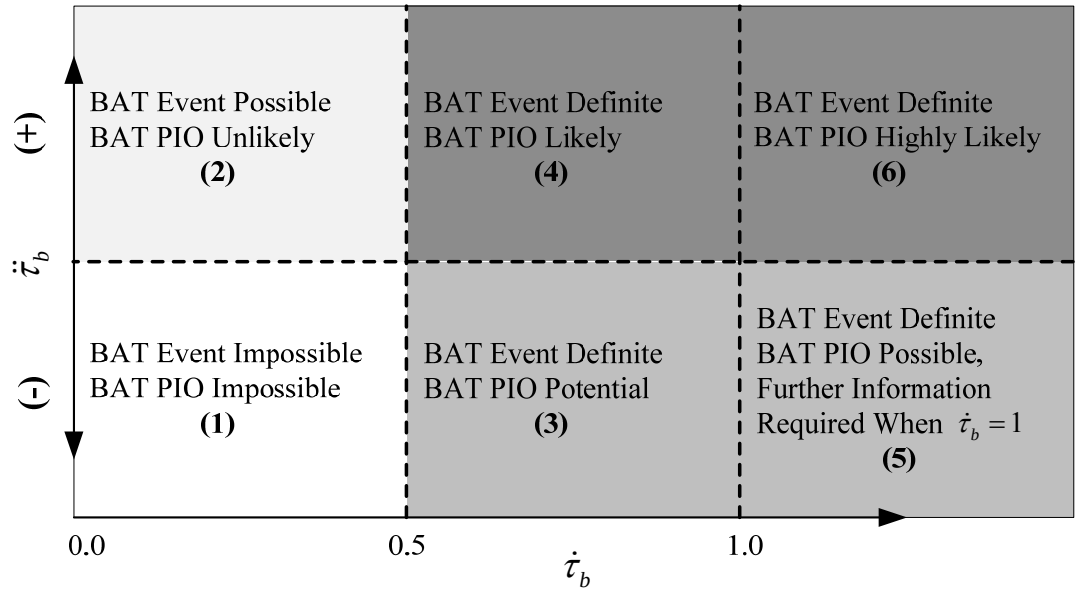

Figure 41: $\dot{\tau}$ and $\ddot{\tau}$ conditions for BAT event and PIO prediction at the reference line [21;22]

The procedure to apply the criteria shown in Figure 41: as a post-processing tool is illustrated in Figure .

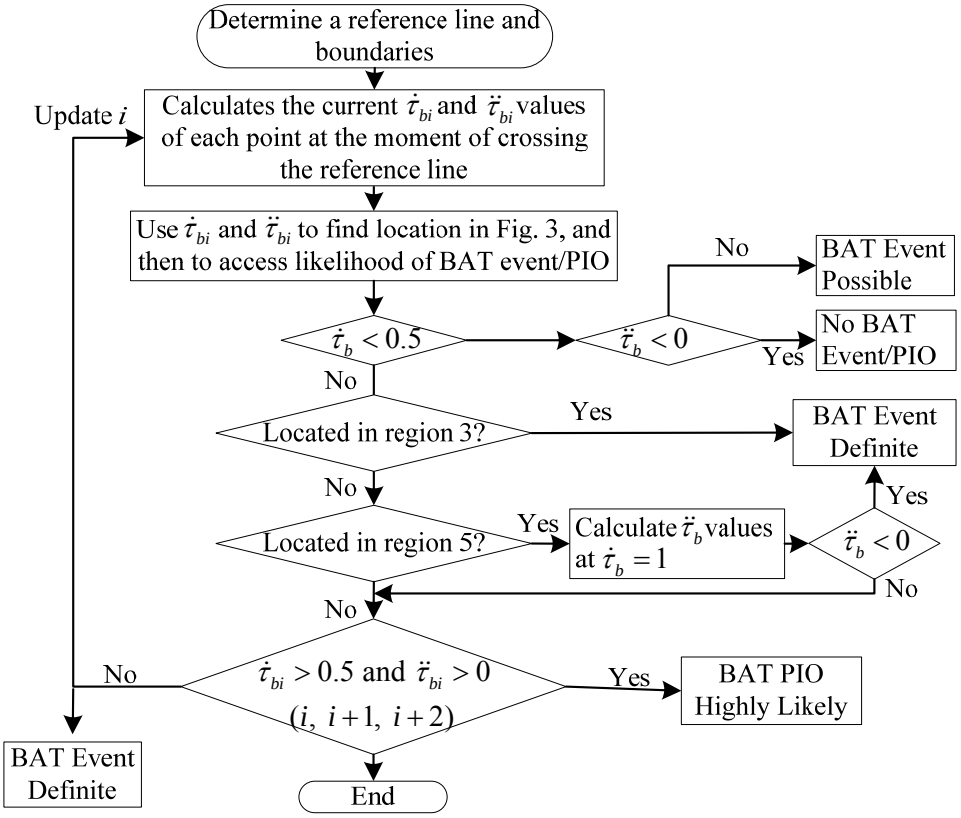

Figure 42*:* Flowchart for the proposed BAT event and PIO prediction method.

The application of the procedure in Figure is straightforward. A reference line is selected. This might, for example, be the object that the pilot initiates the deceleration phase to avoid (an impending boundary) or the object/parameter that the pilot is following using a point tracking strategy. For example, a runway edge was selected for the roll-step manoeuvre of the previous research activity. Once the parameter being tracked deviates from the reference, the next step is to calculate the instantaneous values of $\dot{\tau}_b$ and $\ddot{\tau}_b$ from the current parameter value to the defined reference. The likelihood of a BAT event or BAT PIO occurring can be predicted based on the location of the result in Figure 41:. Of particular interest, however, is if the result of the analysis is contained within region 5 of Figure 41:. Because such results suggest that the aircraft is accelerating toward to the boundary ($\dot{\tau}_b > 1.0$, though their $\dot{\tau}_b$ values are reducing ($\ddot{\tau}_b < 0$)). Further information is required to know how rapidly $\dot{\tau}_b$ will decrease as the boundary is approached. The moment that is critical when describing the change between acceleration and deceleration towards a boundary ($\dot{\tau}_b = 1$) is therefore selected and analysed further. To avoid the method generating a large number of false positive BAT PIO predictions, the suggested convention to be adopted is to only flag a BAT PIO as being in progress when 3 consecutive data points are located in regions (4) and (6). This may be conservative but the user is free to modify this convention depending upon the specific configuration of an experiment.

2.5 Prediction based on Bifurcation Analysis

Bifurcation theory considers the Pilot-Vehicle System (PVS) nonlinear and therefore the motion of such system is composed of “fixed points” and “periodic orbits” (“limit cycles”) [35;36]. The stability of a fixed point and periodic orbit when a system’s parameter is varied results in fixed-point and periodic orbit bifurcations. The different kind of bifurcations from fixed points and from periodic orbits is of interest for A/RPC study. A good explanation of bifurcation theory as applied to APCs is given in GARTEUR FM AG-12 [37]. Bifurcation theory has been applied to APC analysis in refs. [37-40]. Ref. [38] considered two kind of nonlinear PVS, namely a linear airframe with a rate limited actuator and an airframe with nonlinear aerodynamics. The limit cycle amplitude was computed as a function of pilot gain, showing a large jump corresponding to the onset of nonlinear effects and PIO. Ref. [39] studied the PIO problem in the aircraft landing transition between the approach task and flare to touch-down. It was shown that, for a PVS system enhanced with a generic FCS, in highly demanding tasks such as the landing, too high at gain in the FCS reduced the pilot’s allowable reaction time to levels where PVS oscillations appeared corresponding to a Hopf bifurcation.

The application of the bifurcation method in ARISTOTEL is aimed at predicting two types of RPC occurrences: Category II PIO due to rate limiting, and BAT RPC. The first step of the bifurcation analysis is the problem formulation: the PVS has to be formulated in a state-space form $\dot{X} = F(X, \lambda)$ where, X is the n-dimensional state vector λ is the m-dimensional parameter vector F is a vector of n nonlinear continuous and differentiable functions.

The next step is the determination of the asymptotic behaviour of the system when the parameters of the system are varying quasi-steadily.

2.5.1 Rate limiting

An approach similar to Mehra and Prasanth’s [38] and GARTEUR FM AG-12’s [40] is used to assess PIO potential, with the following steps:

- Formulate a limit cycle and bifurcation problem for the PVS by augmenting the PVS with a nonlinear oscillator as the command input. Compute bifurcation surfaces and limit cycles as a function of pilot gain and rate limit.

-Check for Hopf bifurcations and jump resonances leading to limit cycles and large jumps in limit cycle amplitude as the pilot gain increases. Flying qualities “cliffs” are associated with these nonlinear phenomena.

The rotorcraft model used is the linearized helicopter models derived from the nonlinear BO105 models implemented in SIMONA (TUD), HELIFLIGHT-R (UoL) and HOST (ONERA). The pilot model used is a crossover model with a pure gain. This assumption is well accepted in the case where the PIO is fully developed (synchronous precognitive behaviour). The closed-loop model of the PVS is presented in Figure 43, including the limitation on the stick deflection and the rate limit element. The PVS is augmented with a command signal generator, represented by a nonlinear oscillator which has the periodic command as an asymptotically stable periodic solution. Indeed, as the PIO must be predicted for any initial conditions, a nonlinear oscillator is required. In state-space form, the proposed oscillator is given by,

$$\dot{x}_1 = A^2 x_1 + \Omega x_2 - \left(x_1^2 + x_2^2\right)x_1$$
$$\dot{x}_2 = -\Omega x_1 + A^2 x_2 - \left(x_1^2 + x_2^2\right)x_2$$

where Ω is the command input frequency and A is the command input amplitude.

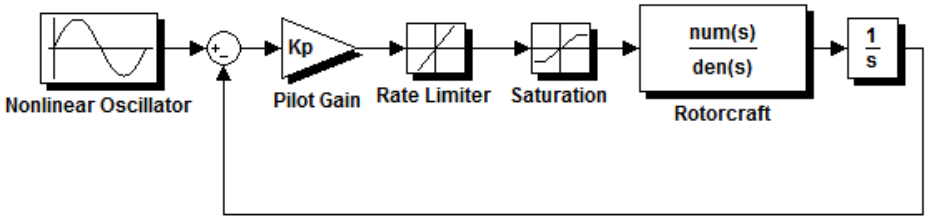

Figure 43: Augmented pilot-vehicle system for Cat II PIO analysis.

It should be noted that the command signal does not correspond necessarily to real piloting tasks intended to trigger PIO, but it constitutes a mathematical trick to make possible the use of standard bifurcation methods. Practically, the worst case should be retained for the command signal. As there is no feedback from the PVS to the oscillator, it can be shown that the global properties of the PVS are the same as those of the augmented system. The augmented system is an unforced dynamical system and can be analysed using standard bifurcation methodology.

The amplitudes of the limit cycles are determined as functions of the rate limits and the pilot gains. The pilot model gains are assumed to be adjusted based on the linear crossover phase angle of the open loop rotorcraft-pilot system Φ_C. Within this study a gain spectrum from $\Phi_C = -110\,\text{deg}$ (low pilot gain) up to $\Phi_C = -160\,\text{deg}$ (high pilot gain) is used. A metric is proposed to measure the PIO susceptibility, given by the derivative of the amplitude of the rotorcraft limit cycle with respect to the rate limit, i.e. $\partial q / \partial r_{\lim it}$ in the pitch axis, and $\partial p / \partial r_{\lim it}$ in the roll axis. It can be interpreted graphically as the slope of the limit cycle amplitude envelope [40].

A sample of the prediction results is presented below with the following formats: 3D plot of helicopter state variables versus rate limits and pilot gains, 3D plot of PIO susceptibility parameter versus rate limits and pilot gains, 2D plot contour of PIO susceptibility parameter.

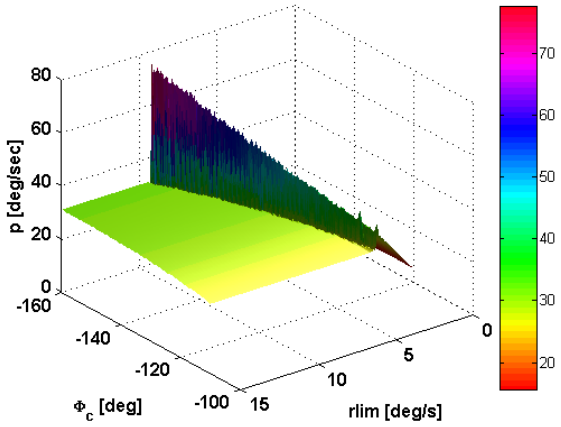

Figure 44a: Envelope of roll rate limit cycles as a function of rate limit and pilot crossover phase angle.

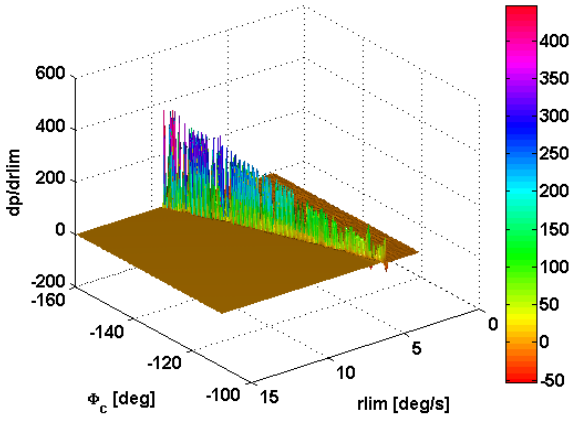

Figure 44b: PIO susceptibility parameter of BO105 in roll as a function of rate limit and pilot crossover phase angle.

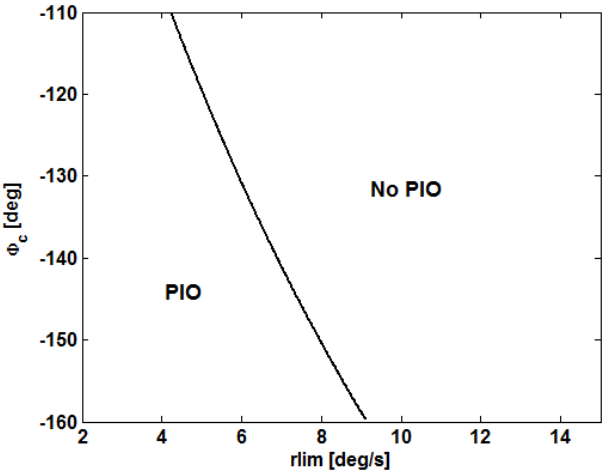

Figure 45: Roll PIO boundary of BO105 based on PIO susceptibility parameter.

In the roll axis, for high rate limits, the amplitude of the PVS system is that of a periodic solution, depending on the command frequency and amplitude. As the rate limit decreases, a Hopf bifurcation is encountered leading to large jumps of limit cycles amplitudes in roll rate (Figure 44a). The jumps are also illustrated by discontinuities in roll derivative $\partial p / \partial r_{\lim it}$ (Figure 44b). The combinations of pilot gains and rate limits for which a large jump in limit cycle amplitude is observed are plotted in Figure 45 as the boundary delimitating regions where the rotorcraft is PIO prone and PIO free. For example, for a pilot crossover phase angle $\Phi_C = -140\,\mathrm{deg}$, this can be already observed for rate limit 6.7deg/s.

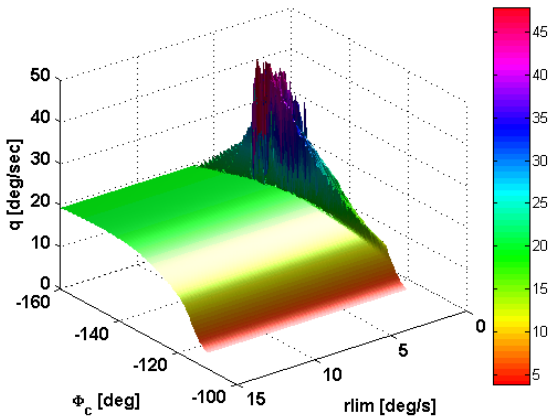

Figure 46a: Envelope of pitch rate limit cycles as a function of rate limit and pilot crossover phase angle.

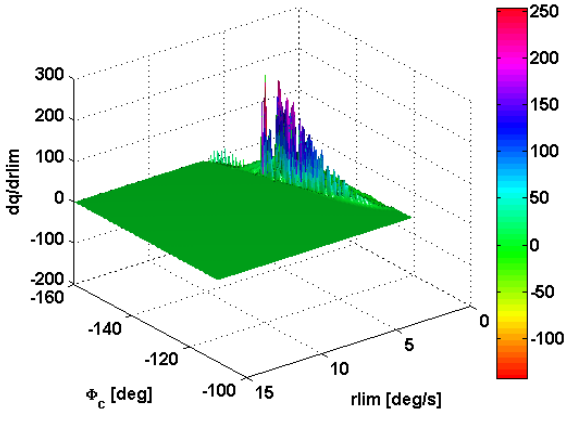

Figure 46b: PIO susceptibility parameter in pitch as a function of rate limit and pilot crossover phase angle.

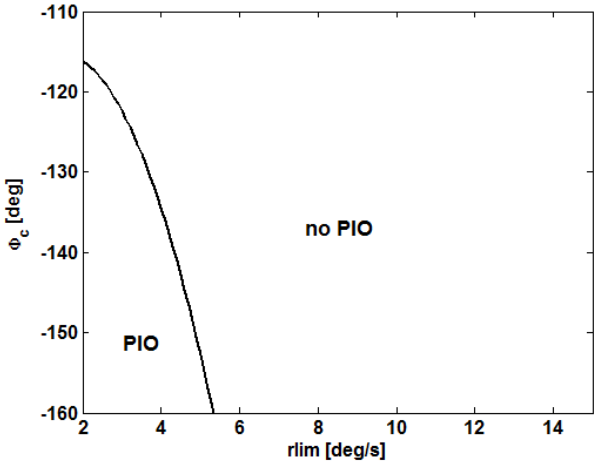

Figure 47: Pitch PIO boundary based on PIO susceptibility parameter

In the pitch axis, for high rate limits, the amplitude of the PVS system is also that of a periodic solution, depending on the command frequency and amplitude. As the rate limit decreases, a Hopf bifurcation is encountered leading to large jumps of limit cycles amplitudes in pitch rate (Figure 46a). The jumps are also illustrated by discontinuities in pitch derivative $\partial q / \partial r_{\lim it}$ (Figure 46b). The combinations of pilot gains and rate limits for which a large jump in limit cycle amplitude is observed are plotted in Figure 47 as the boundary delimitating regions where the rotorcraft is PIO prone and PIO free. For example, for a pilot crossover phase angle $\Phi_C = -140\,\mathrm{deg}$, this can be already observed for rate limit 4.3deg/s.

The data and PIO Ratings (PIOR) collected during the 1st test campaign on the TUD SIMONA and the HELIFLIGHT-R simulators [3] are used for the assessment of the bifurcation analysis. The tasks considered are the roll tracking task and the pitch tracking task. The assessment of the bifurcation analysis is dependent on the pilot gain. In the correlation procedure, it was assumed a fixed crossover phase of -140deg. The effectiveness of the analysis method in predicting PIO can be evaluated according to the following performance metrics: 1/ Global success rate I1 = percentage of cases which are correctly predicted to be PIO free or prone. 2/ Index of conservatism I2 = percentage of cases predicted PIO prone which have actually undergone PIO in reality with respect to the total number of predicted PIO prone cases. 3/ Safety index I3 = percentage of cases which are predicted by the criterion to be PIO prone, with respect to the total number of simulator test PIO cases.

Table 5: Assessment of bifurcation analysis

Tasks	I1	I2	I3
Pitch tracking	80%	62%	83%
Roll tracking	93%	50%	50%

From the results displayed in Table 5, it can be seen that

- In the pitch axis the performance of the bifurcation analysis is comparable to OLOP [5].
- In the roll axis, the very low number of runs (2) for the 5deg/sec rate limit-configuration tested does not allow a significant assessment of the method for that

configuration, as it was also for OLOP [5]. The safety index is equal to 50% due to the fact that while the criterion predicts a PIO prone configuration, one run was awarded PIOR 1 and the other PIOR 4.

2.5.2 Boundary Avoidance Tracking

The emphasis in this type of RPC occurrences was on predicting RPC due to switching control modes between Point Tracking (PT) and Boundary Avoidance Tracking (BAT). Two tracking tasks have been considered: the roll step manoeuvre and the pitch tracking task. Concerning the roll step manoeuvre, the stability analysis has been reported in the deliverable D2.7. No correlation with tests data was made as no BAT event was encountered during the 1st test campaign [3]. A summary of analysis and off-line simulation is only recalled below. Concerning the pitch tracking task, the stability analysis is more detailed hereafter and the identification of the combined PT-BAT pilot model is presented by using the test data of the 2nd campaign [4].

Roll step manoeuvre

The roll step manoeuvre is described as follows: the helicopter is initially flown along one edge of a runway. The piloting task consists of traversing the runway to reach the other edge over a specified distance and fly through a series of gates (the boundaries). The PT pilot model is formulated as PID controller, and the boundary avoidance strategy is given by Gray's model [13]. It was searched the combinations of the model parameters that drive the pilot-vehicle system into instability. The parameters selected in Gray's model are the minimum time to boundary Tmin at which the pilot starts to respond to the boundary, and the maximum time to boundary Tmax at which the pilot applies the maximum boundary gain to avoid reaching the boundary. The stability analysis of the coupled pilot-vehicle system are detailed in the deliverable D2.7, the main results are recalled hereafter. Figure 48 presents the combinations of Tmin and Tmax which delimitate regions of stable/unstable motion based on the analysis of the asymptotic behaviour of the closed loop pilot-vehicle system.

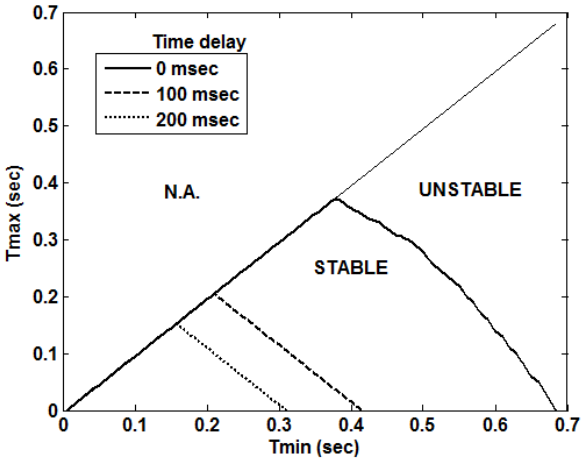

Figure 48: Bifurcation surface of a PT/BAT pilot-BO105 system performing a roll step manoeuvre. Influence of additional time delay.

According to the definition of Tmin and Tmax, one has to consider only the area on the figure corresponding to Tmax<Tmin. The straight borderline Tmax=Tmin represents a pilot who switches instantaneously from the PT mode to the BAT mode as time to boundary decreases, while the borderline Tmax=0 (i.e. the Tmin-axis) represents a pilot who proceeds

gradually. Any point inside the area delimited by the bifurcation surface is stable. It is evident that a real pilot will not keep constant Tmin and Tmax during the task but will adopt rather an adaptive strategy. The bifurcation method which is based on the analysis of the asymptotic behaviour of the closed-loop pilot-vehicle system cannot predict this strategy nor the effects due to transients. However, as long as the strategy leads to a combination of (Tmin, Tmax) inside the region of stability, the system is expected to be BAT RPC free. The influence of additional time delay on the region of stability is also presented on the figure. As expected, increasing the time delay reduces the region of stability.

An off-line simulation of the roll step manoeuvre is presented in Figure 49, where the time histories of the helicopter response and control deflections are plotted. Minimum time to boundary and maximum time to boundary were fixed to Tmin = 0.20s and Tmax = 0.12s respectively. An additional time delay of 200ms was introduced in the system. The above combination of parameters corresponds to a point on the 200ms-bifurcation surface of Figure 48, and as predicted, the pilot-vehicle system exhibits a sustained oscillation (Figure 49).

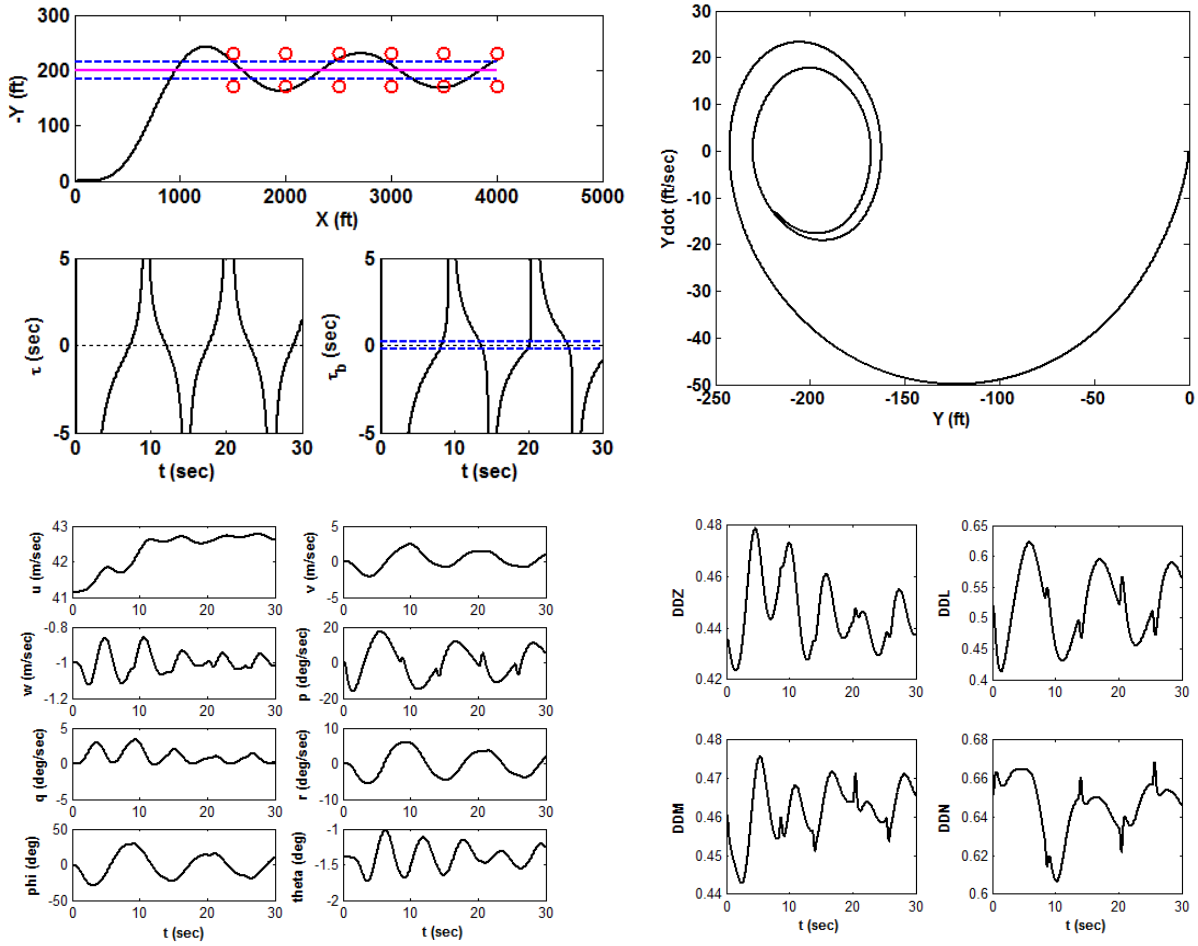

Figure 49: Simulation of BAT RPC of the BO105 during a roll step manoeuvre. Time delay is 200ms. Notations – u, v, w body-axes airspeed components – p, q, r roll, pitch, yaw rates – phi theta roll, pitch angles – DDZ DDL DDM DDN collective, lateral stick, longitudinal stick, pedals

Pitch tracking manoeuvre

In the pitch tracking task the pilot is required to track in the head-up-display a marker which oscillates in pitch between two boundaries. The boundaries are narrowed progressively with the aim to trigger BAT RPC. To reduce the predictability of the marker path, a sum of sine functions of different frequency is used to generate the tracking signal.
The rotorcraft model used is the linearized helicopter model around 80kts forward flight, derived from the nonlinear BO105 model implemented in the HELIFLIGHT-R simulator (UoL):

$$\dot{x} = Ax + Bu$$

The number of degrees of freedom for linearization is as follows [2]:

```
A matrix
States x
(:,1) = phi
(:,2) = theta
(:,3) = main rotor 1 flap
(:,4) = main rotor 2 flap
(:,5) = main rotor 3 flap
(:,6) = main rotor 4 flap
(:,7) = u
(:,8) = v
(:,9) = w
(:,10) = p
(:,11) = q
(:,12) = r

B matrix
Controls u
(:,1) = lateral (XA)
(:,2) = longitudinal (XB)
(:,3) = collective (XC)
(:,4) = pedals (XP)
```

A crossover pilot model is used for PT, and Gray's model [13] is used for BAT. It is searched the combinations of the model parameters that drive the pilot-vehicle system into instability. The longitudinal control XB generated by the combined PT/BAT pilot model is a linear combination of PT control and BAT control through the BAT gain Km:

$$XB = (1 - K_m) XB_{PT} + K_m XB_{BAT}$$

Figure 50a shows the root locus of the linearized coupled pilot-BO105 system in a pitch tracking task, when the BAT gain parameter Km is varying quasi-steadily from 0 to 1. The crossover phase angle of the PT model is equal to -140deg.

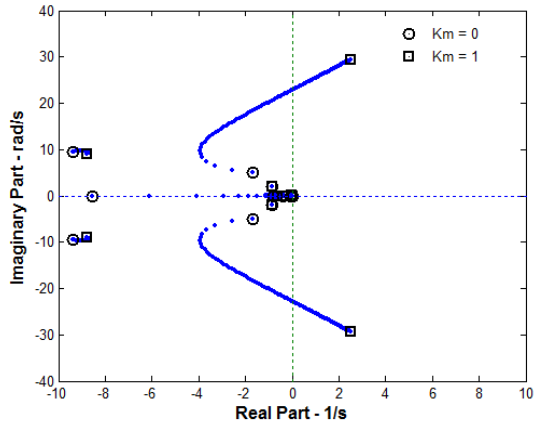

Figure 50a: PT/BAT pilot-BO105 root locus.

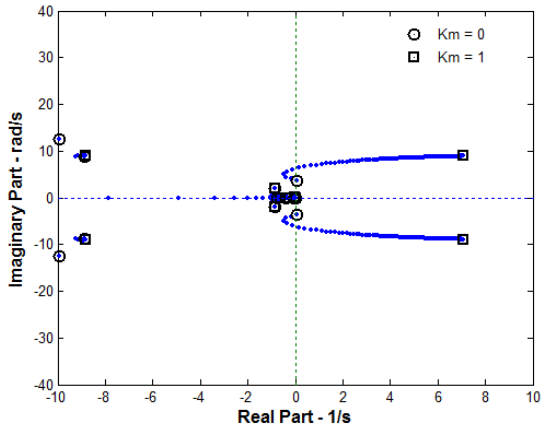

Figure 50b: PT/BAT pilot-BO105 root locus. Additional time delay 200ms.

As a pair of complex eigenvalues cross the imaginary axis of the complex plane, a Hopf bifurcation occurs in the dynamical system. Stability is lost and from there, the steady point of the PT piloting mode gives birth to a stable limit cyclic.
Figure 50b shows the root locus when an additional time delay of 200ms is introduced in the system. The BAT gain Km for which the system starts to enter a limit cycle is considerably reduced.

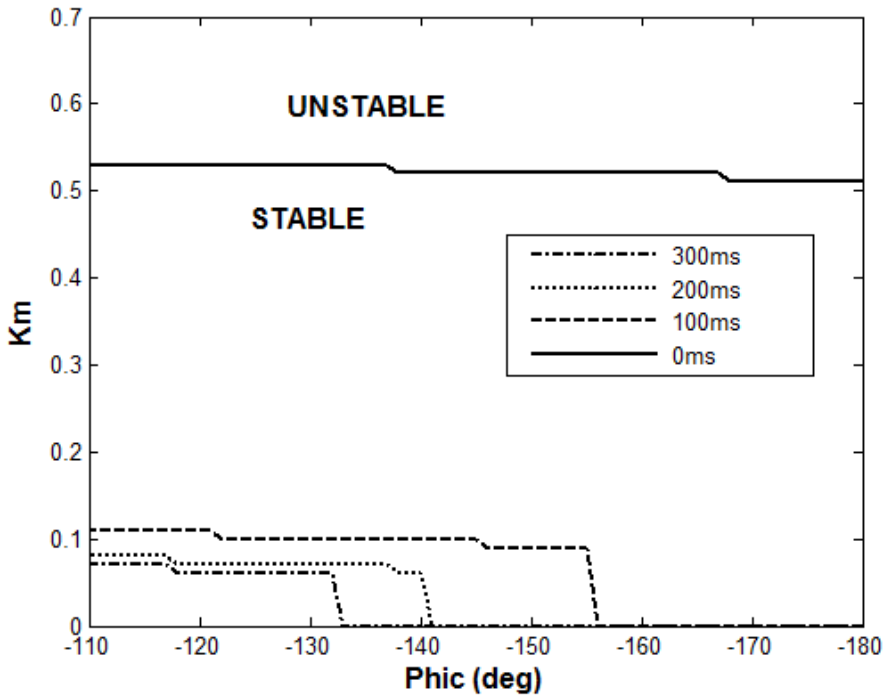

Figure 51: Bifurcation surface of a PT/BAT pilot-BO105 system performing a pitch tracking task. Influence of additional time delay.

Figure 51 presents the bifurcation surface in the parameter space (Phic, Km) which delimitates the region of stability. Phic is the crossover phase of the PT model and Km is the

BAT gain. The influence of additional time delay on the region of stability is also shown. As expected, increasing the time delay reduces the region of stability. Below -180deg of Phic, the system is unstable for any gain Km. It is evident that a real pilot will not keep constant Phic and Km but will adopt rather an adaptive strategy. The method based on the analysis of the asymptotic behaviour of the closed-loop pilot-vehicle system cannot predict this strategy nor the effects due to transients. However, as long as the strategy leads to a combination of (Phic, Km) inside the region of stability, the system is theoretically BAT RPC free.

The above theoretical PT/BAT model is used to simulate a BAT tracking task which was performed on the HELIFLIGHT-R simulator during the 2nd test campaign [4]. For the case study presented here, the helicopter model has an additional time delay of 200ms. A run consisted of tracking a reference signal θ_d in repeated sequences, the first sequence having the widest boundaries and the last one having the narrowest boundaries.
The parameters of the PT crossover model

$$XB_{PT} = -K_p\left(\theta - K_{lead}\theta_d\right)$$

are identified using the first tracking sequence. Indeed, it is assumed that the pilot uses a PT strategy when the boundaries are wide enough.
For the sample of simulator test run presented below, the gains identified are Kp = 12.59, which corresponds to a crossover phase of -129deg, and Klead = 0.9. The pitch response of the helicopter to the PT model and the response from the simulator test are plotted in Figure 52a.

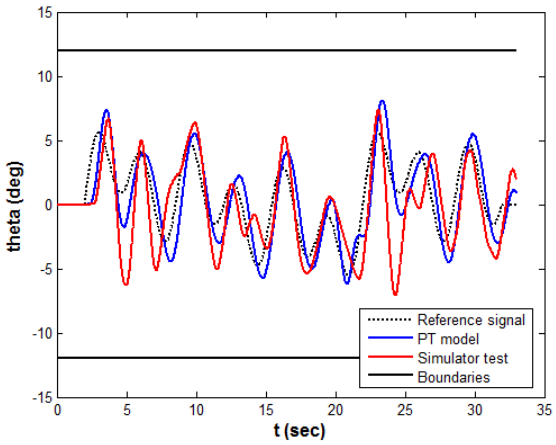

Figure 52a: Pitch response to PT pilot model in the first tracking sequence.

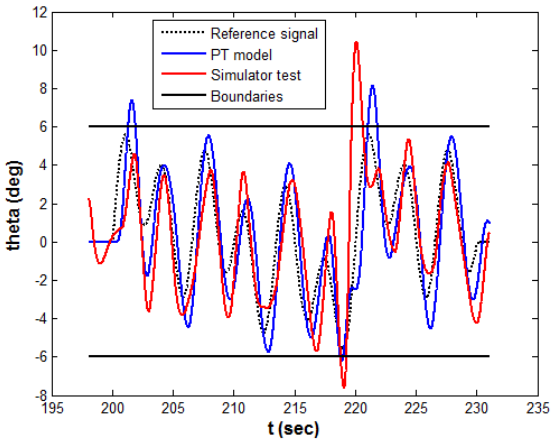

Figure 52b: Pitch response to PT pilot model in the last tracking sequence.

Figure 52b displays the pitch response assuming that the PT model remains unchanged in the last tracking sequence where the boundaries are narrowed. As expected, the PT model does not reflect the avoidance strategy applied by the pilot during the simulator test. This can be observed for example on the first peak of the oscillations.
Figure 53 presents the pitch response in the last tracking sequence for a combined PT-BAT model with fixed gains in the PT model (Kp = 12.59, Klead = 0.9), and fixed parameters in the BAT model (Tmin = 1.2s, Tmax = 0.1 s, and XBBAT = 0.1).

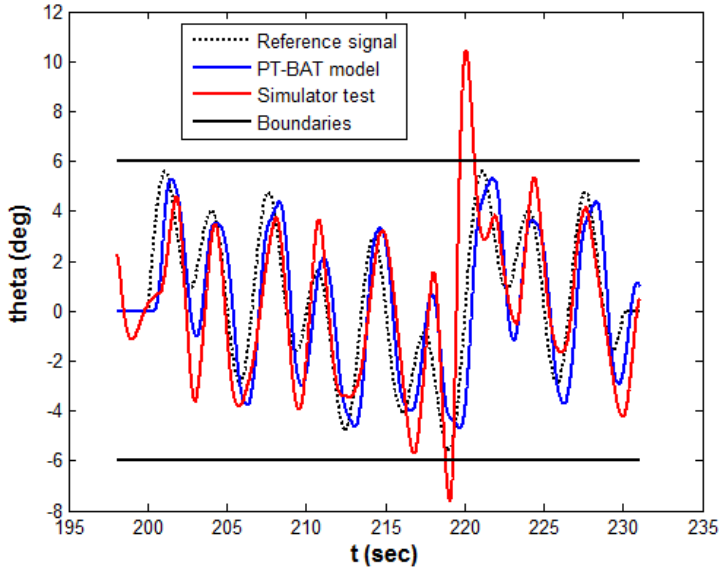

Figure 53: Pitch response to PT-BAT pilot model in the last tracking sequence.

It can be seen that the boundaries avoidance is now roughly reproduced by the model. To reproduce the boundaries violations at t = 219s and t = 220s made by the pilot on the simulator, it is assumed that the pilot has increased his BAT gain in this time interval. Figure 51 shows indeed that a high BAT gain leads to instability. Figure 54 presents the pitch response in the last tracking sequence for a combined PT-BAT model with the same previous values of the parameters, except in the [219s; 221s] time interval:

- Tmin = 2s, Tmax = 0.1 s, and XBBAT = 4 in the [219s; 219.5] time interval
- Tmin = 6s, Tmax = 0.1 s, and XBBAT = 0.1 in the [220s; 221s] time interval.

As shown in Figure 54, the boundaries violations are well reproduced by the model.

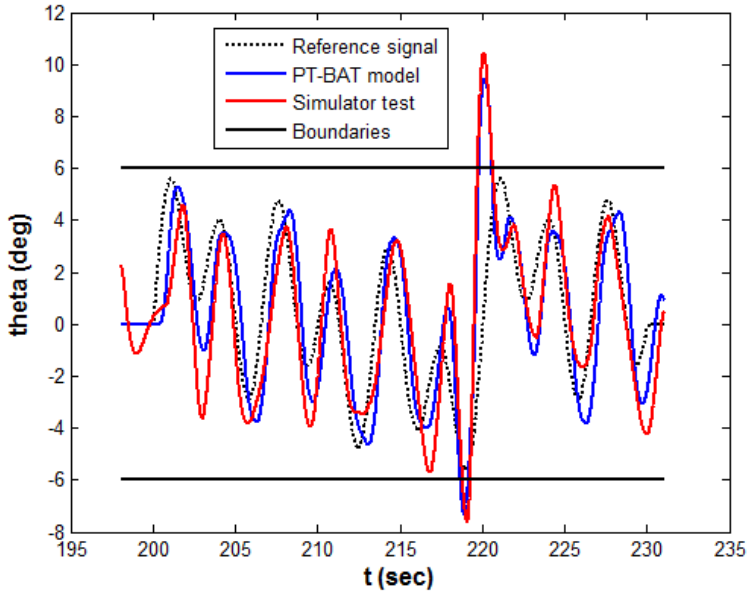

Figure 54: Pitch response to PT-BAT pilot model with variable BAT gain in the last tracking sequence.

3. Conclusions

Among the numerous criteria that have been elaborated in the past for fixed-wing APC prediction, the existing state-of-the-art in RPC prediction relies mainly on the bandwidth criterion which has been adapted and added as quantitative requirements in the ADS-33 helicopter handling qualities specification for Cat I RPC prediction. The work performed over the course of the ARISTOTEL project has brought significant progress beyond the state-of-the-art in RPC prediction and detection:

- The Real-Time Oscillation Verifier (ROVER) tool for on-line PIO detection was adapted to helicopters and the algorithm of the “peak selection” within this tool was enhanced for an improved detection of RPC occurrences. Furthermore, the ROVER tool was coupled to the ADS-33 bandwidth phase delay criterion in order to allow for a correlation of ROVER with the HQs degradation

- A new on-line detection algorithm, the so-called Phase Aggression Criterion (PAC) was proposed in the project for Cat II PIO detection. PAC achieves a 'detection' of an A/RPC through the observation of the phase distortion between the PVS and the pilot input rate. Observing pilot input allows one to check that the pilot is coupled with the oscillations (a pre-requisite for PIO) whilst the phase difference allows one to see whether the commanded input is in-phase with the vehicle response. The combination of the two parameters at a finite point in time allows one to objectively assess whether an A/RPC has materialised.

- A new off-line prediction criterion, the so-called PRE-Phase Aggression Criterion (PRE-PAC) was proposed in the project. For this, one needs first to pre-define input signals to be fed into a simulation model. These have to be designed to account for a range of active pilot control inputs. Then, one needs to determine the time dependent ‘Phase’ and ‘Aggression’ parameters for each input signal, by running a simulation in the time domain. These results are then used to determine the systems incipience to RPC. In the project, through a number of piloted simulation campaigns, severity boundaries have been defined in charts representing the Aggression parameter (deg/s^2) as a function of the phase distortion parameter (deg).

- The state-of-the-art in using the so-called Boundary Avoidance Tracking (BAT) to predict RPCs was advanced. BAT considers that during an A/RPC event, the pilot behaviour is different from the assumed point tracking (PT) flight behaviour and is more like tracking and avoiding a succession of opposing events which can be described as boundaries. The project assessed the characteristics of the pitch tracking features under the variation of the boundary size showing that the smaller the boundary size the narrower is the safe region.

- The Optical Tau theory was applied to predict BAT RPC. Tau theory is based upon the premise that purposeful actions are accomplished by coupling the motion under control with either externally or internally perceived motion variables. With the hypothesis that the pilot closed the aircraft motion gaps by following a constant deceleration guide, the research bringing together optical tau and BAT has found that

roll-step control can be modelled as a prospective strategy by coupling lateral motion onto an intrinsic tau guide, taking the form of the constant deceleration.

- Bifurcation analysis was applied to detect Cat II RPC (rate limiting) and to a BAT system performing a roll step manoeuvre and a pitch tracking manoeuvre.

The data generated from 2 test campaigns on the SIMONA simulator and 2 test campaigns on the HELIFLIGHT-R simulator have been used to assess the traditional prediction criteria (Bandwidth-Phase Delay, Open Loop Onset Point) as well as the newly developed prediction tools. Further experimental investigations are suggested to consolidate the validation.

4. References

[1] ARISTOTEL, Annex I – Description of work, Jun. 2010.

[2] ARISTOTEL, Revised database of RPC predictions, Deliverable D2.7, Dec. 2012.

[3] ARISTOTEL, Simulator test data analysis of the 1st test campaign, Deliverable D4.6, Jun. 2012.

[4] ARISTOTEL, Simulator test data analysis of the 2nd test campaign, Deliverable D4.8, Sept. 2013.

[5] ARISTOTEL, Results of rigid body model validation exercise, Deliverable D4.9, Dec. 2012.

[6] Mitchell, D.G., PIO Detection with a Real-time Oscillation Verifier (ROVER), Viewgraphs presented at NASA Dryden Flight Research Center, April 8th, 1999. NASA/CP-2001-210389/Vol.2

[7] Mitchell, D.G., A.J. Arencibia and S. Munoz: „Real-Time Detection of Pilot-Induced Oscillations“, AIAA-04-4700 Atmospheric Flight mechanics Conference, Providence, RI, 16-19 August 2004

[8] GARTEUR FM(AG12), Investigation of Methods for On-Line PIO Detection, TP-120-09, 2002

[9] Mariano,V., G. Guglieri and A. Ragazzi: Application of pilot induced oscillations prediction criteria to rotorcraft, 37th European Rotorcraft Forum, Varese, September 13 – 15, 2011

[10] Suliman, S. ,Yilmaz, D. and Pavel, M. Harmonizing the Realtime Oscillation Verifier (ROVER) with Handling Qualities Assessment for Enhanced Rotorcraft Pilot Couplings Detection, Proceedings of the 38th European Rotorcraft Forum, Amsterdam, Netherlands, 2012

[11] Jones, M., Jump, M., Lu, L., A new method for near real-time rotorcraft pilot coupling detection and identification. Journal of Guidance, Control and Dynamics 2012;35(1):80–92.

[12] Anon., Aeronautical Design Standard Performance Specification Handling Qualities Requirements for Military Rotorcraft, United States Army Aviation and Missile Command Aviation Engineering Directorate, Redstone Arsenal, Alabama, 2000.

[13] Gray III, W. R., Boundary-Avoidance Tracking: A New Pilot Tracking Model, AIAA Atmospheric Flight Mechanics Conference and Exhibit, San Francisco, California, Aug., 2005, pp. 86-97.

[14] Lee, D. N., Guiding Movement by Coupling Taus, Ecological Psychology, published online 1998; Vol. 10, No. 3, pp. 221-250.

[15] Gibson, J. J., The Perception of the Visual World, American Journal of Psychology, Vol. 64, 1951, pp. 622-625.

[16] Jones, M., Jump, M., Lu, L., Pavel, M., and Yilmaz, D., “The Use of the Phase-Aggression Criterion for Identification of Rotorcraft Pilot Coupling Events,” 38th European Rotorcraft Forum, Amsterdam, Netherlands, Sept. 4th-7th 2012.

[17] Hess, R.A., Simplified Approach for Modelling Pilot Pursuit Control Behaviour in Multi-Loop Flight Control Tasks, Proceedings of the I MECH E Part G Journal of Aerospace Engineering, published online 2006; Vol. 220, No. 2, pp. 85-102.

[18] Hess, R.A., Obtaining Multi-Loop Pursuit-Control Pilot Models From Computer Simulation, Proceedings of the I MECH E Part G Journal of Aerospace Engineering, published online Feb. 2008; Vol. 222, No. 2, pp. 189-199.

[19] Hess, R.A., and Siwakosit, W., Assessment of Flight Simulator Fidelity in Multiaxis Tasks Including Visual Cue Quality, Journal of Aircraft, published online Jul. 2007; Vol. 38, No. 4, pp. 607-614.

[20] Hess, R. A., and Marchesi, F., Analytical Assessment of Flight Simulator Fidelity Using Pilot Models, Journal of Guidance, Control, and Dynamics, published online May. 2009; Vol. 32, No. 3, pp. 760-770.

[21] Gray III, W. R., Handling Qualities Evaluation at the USAF Test Pilot School, Proceedings of the AIAA Atmospheric Flight Mechanics Conference 10 - 13 August 2009, Chicago, Illinois.

[22] Warren, R. D., An Investigation of the Effects of Boundary Avoidance on Pilot Tracking, Air Force Inst. of Tech., Wright-Patterson AFB, OH. Graduate School of Engineering and Management, Dec., 2006.

[23] McRuer, D. T., and Krendel, E. S., Mathematical Models of Human Pilot Behavior, AGARD-AG-188, Jan.1974.

[24] McRuer, D. T., Clement, W. F., Thompson, and R. E. Magdaleno, Minimum Flying Qualities Volume II: Pilot Modelling For Flying Qualities Application, Flight Dynamics Laboratory, Air Force Systems Command, Wright-Patterson Air force Base, OHIO,WRDC-TR-89-3125, Jan.1990.

[25] McRuer, D. T., Pilot-Induced Oscillations and Human Dynamic Behavior, NASA Contractor Report 4683, Jul.1995.

[26] Jump, M., Hodge, S., Dang Vu, B., Masarati, P., Quaranta, G., Mattaboni, M., Pavel, M. D., and Dieterich, O., Adverse Rotorcraft-Pilot Coupling: Test Campaign Development at the University of Liverpool, 34th European Rotorcraft Forum, Liverpool, England, Sept. 16th -18th 2008.

[27] Blake, R.D. Boundary Avoidance Tracking: Consequences (and Uses) of Imposed Boundaries on Pilot-Aircraft Performance, MSc Thesis, Department of the Air Force, United States Air Force Institute of Technology, Wright-Patterson Air Force Base, Ohio, 2009.

[28] Dotter, J. D., An Analysis of Aircraft Handling Quality Data Obtained From Boundary Avoidance Tracking Flight Test Techniques, Air Force Inst. of Tech., Wright-Patterson AFB, OH. Graduate School of Engineering and Management, Mar., 2007.

[29] McRuer, D. T., et al., Aviation Safety and Pilot Control Understanding and Preventing Unfavourable Pilot-Vehicle Interactions, National Academy Press, ASEB National Research Council, Washington D.C., 1997.

[30] White, M. D., Perfect, P., Padfield, G. D., Gubbels, A. W., and Berrayman, A. C., Acceptance Testing of A Rotorcraft Flight Simulator for Research and Teaching: the Importance of Unified Metrics, 35th European Rotorcraft Forum, Hamburg, Germany, Sept. 22th - 25th 2009.

[31] Lampton., A., and Klyde, D. H., Power Frequency: A Metric for Analyzing. Pilot-in-the-Loop Flying Tasks, Journal of Guidance, Control, and Dynamics, published online Sept. 2012; Vol. 35, No. 5, pp. 1526-1537. doi: 10.2514/1.55549.

[32] Allen, R. W., Clement, W. F., and Jex, H. R., Research on Display Scanning, Sampling, and Reconstruction Using Separate Main and Secondary Tracking Tasks, NASA Contractor Report CR-1569, NASA Contractor Report CR-1569, Jul. 1970.

[33] Lu, L., Padfield G.D., and Jump, M. Optical tau in boundary-avoidance tracking - a new perspective on pilot-induced oscillations, 36th European Rotorcraft Forum, Sept. 6th - 9th, Paris, France, 2010.

[34] Padfield G.D., Lu, L., and Jump, M., Tau guidance in boundary-avoidance tracking - new perspectives on pilot-induced oscillations, J Guid Contr Dynam, accepted for publication, 2011.

[35] Ioos, G. and Joseph, D.D., Elementary Stability and Bifurcation Theory. Springer Verlag, 1981.

[36] Marsden, J.E. and Mc Cracken, M., The Hopf Bifurcation and its Applications. Springer Verlag, 1976.

[37] GARTEUR FM AG-12, Analysis of Nonlinear Pilot-Vehicle System Using Modern Control Theory, TP-120-02, 2001.

[38] Mehra, R.K., Prasanth, R.K., Bifurcation and Limit Cycle Analysis of Non-linear Pilot, AIAA Paper 98-4249, 1998.

[39] Halanay, A., Ionita, A., Safta, C.A., Hopf Bifurcations through Delay in Pilot Reaction in a Longitudinal Flight, Nonlinear Dyn, No 60, pp 413–423, 2010.

[40] GARTEUR FM AG-12, PIO Analysis of a Highly Augmented Aircraft, TP-120-07, 2001.

[41] Johnson, D. A.: `Suppression of Pilot-induced Oscillation (PIO)', M.S. Thesis. Aeronautics and Astronautics Dept., Air Force Institute of Technology, Wright-Patterson Air Force Base, OH, 2002

5. List of Abbreviations

APC	Aircraft Pilot Couplings
BAT	Boundary Avoidance Tracking
BPD	Bandwidth Phase Delay
OLOP	Open Loop Onset Point
PAC	Phase Aggression Criterion
PIO	Pilot Induced Oscillations
PIOR	PIO Rating
PST	Peak Selection Thresholds
PT	Point Tracking
PVS	Pilot Vehicle System
ROVER	Real-time Oscillation Verifier
RPC	Rotorcraft Pilot Couplings
WP	Work Package